Journal of Computational Science 85 (2025) 102507

Contents lists available at ScienceDirect

Journal of Computational Science

journal homepage: www.elsevier.com/locate/jocs

PDE-LDDMM meets NODEs: Introducing neural ordinary differential equation solvers in PDE-constrained Large Deformation Diffeomorphic Metric Mapping ☆

Monica Hernandez

University of Zaragoza, Aragon Institute on Engineering Research (I3A), Spain

ARTICLE INFO

Keywords:
Neural ordinary differential equations
Large Deformation Diffeomorphic Metric Mapping
Diffeomorphic registration

ABSTRACT

Non-rigid image registration is a crucial task in various medical applications, allowing the alignment of images with complex spatial or temporal variations. This paper introduces NODEO-LDDMM and NODEO-PDE-LDDMM, two innovative deep-learning-based approaches that bridge the gap between Large Deformation Diffeomorphic Metric Mapping (LDDMM) and neural ordinary differential equations (NODEs). LDDMM and PDE-LDDMM offer mathematically well-established formulations for diffeomorphic registration, while NODEs provide the flexibility of deep-learning in the solution of the ODEs involved in both methods. Both NODEO-LDDMM and NODEO-PDE-LDDMM include the strengths of deep-learning into LDDMM, enabling a robust optimization with a good balance between accuracy and transformation smoothness in their solutions. Our proposed methods reached or outperformed their traditional counterparts and the nearly diffeomorphic deep-learning-based approaches selected as benchmarks. This work contributes to advancing non-rigid image registration techniques, with a methodology suited to overcome some of the limitations of deep-learning in medical image registration.

1. Introduction

The non-rigid registration of images is the process of determining the transformation that best warps the source image into the target image according to convenient non-rigid transformation models and image similarity metrics. Non-rigid image registration is a fundamental stage in many different medical applications involving spatial or temporal changes of anatomical or functional features [1–3].

The variational formulation of the non-rigid registration problem from the minimization of an energy functional was inspired by Horn and Schunck method to solve optical flow [4]. The solutions to the non-rigid registration and optical flow problems have evolved through decades, retaining the energy minimization approach as a backbone [3]. Large Deformation Diffeomorphic Metric Mapping (LDDMM) stands out for being a mathematically well-established approach to the non-rigid registration problem through diffeomorphisms [5]. Diffeomorphisms enable shape analysis from transformations and thus, they constitute the inception point of Computational Anatomy [6,7]. The registration quality, the high accuracy, and the convenience of smooth and invertible transformations for medical applications [8] have made diffeomorphic registration the target to reach by many research on non-rigid registration (e.g., the diffeomorphic versions of Demons [9] are preferred over Demons [10]).

The family of PDE-constrained LDDMM methods proposed in [11] and improved in [12,13] is especially interesting. PDE-LDDMM extends the ideas of optical Stokes flow [14] to the diffeomorphic setting. PDE-LDDMM has been used for modeling compressible and incompressible diffeomorphisms, boundary-preserving nonlinear Stokes fluid diffeomorphisms, and mass and intensity preserving diffeomorphisms [13, 15]. The main acknowledged drawback of both LDDMM and PDE-LDDMM is in their time complexity, which is in the order of several minutes for the most interesting models despite the substantial reductions of the computational complexity yielded by the stationary or the band-limited parametrizations [16,17].

Since the deep-learning explosion taking place in the second decade of the XXI century, deep-learning solutions have been proposed to solve a variety of computer vision and medical imaging problems. FlowNet [18] provided the first deep-learning solution to the optical

---

☆ This work was partially supported by the national research grants PID2019-104358RB-I00 (DL-Ageing project, Spain), PID2022-138703OB-I00 (Trust-B-EyE project), RICORS network of inflammatory diseases, Spain RD24/0007/0022 form Carlos III Health Institute, Government of Aragon, Spain grant PROY_B50_24, and Government of Aragon Group Reference, Spain T64_23R (COS2MOS research group).

E-mail address: mhg@unizar.es.

https://doi.org/10.1016/j.jocs.2024.102507
Received 24 May 2024; Received in revised form 6 December 2024; Accepted 8 December 2024

flow problem and the working ideas were quickly adapted and extended to the problems of non-rigid and diffeomorphic registration in medical imaging [19,20]. Supervised deep-learning led to unsupervised approaches for non-rigid and diffeomorphic registration that circumvented the costly need to compute ground truth transformations for training and achieved inference times in the order of a few seconds [21,22].

In this case, the main limitation of unsupervised methods lies in the huge amount of data, the prohibitive hardware requirements, and the energy consumption needed during training. In addition, there are problems with their generalization capability and there is a lack of guarantee that the solution for an image pair belongs to the transformation model even though solid clues that the model can be considered to converge are provided.

Neural Ordinary Differential Equation based Optimization (NODEO) for deformable image registration was recently proposed as a fresh deep-learning approach to the problem of non-rigid and diffeomorphic registration [23]. This method is based on neural ordinary differential equations (NODEs) [24], a promising approach in the field of Scientific Computing cross-fertilized with machine learning to model ordinary differential equations using neural networks [25]. NODEO departs from the LDDMM energy minimization problem and proposes the use of a NODE for the solution of the transport equation. This way, stochastic gradient descent leads the optimization of the loss function which allows to learn the model for the right-hand-side of the transport equation using an implicit neural representation, and, by solving the corresponding ODE, the solution to the image registration problem. With NODEO, learning is specific to every image pair and the hardware requirements are greatly reduced during training. The nature of the approach increases the guarantee that the solution gets close to the transformation model. Overall, NODEO has shown exceptional accuracy at the cost of increasing the computational time to the order of minutes. NODEO source code is available in the GIT repository https://github.com/yifannnwu/NODEO-DIR. From a deep analysis of NODEO (method formulation and codes), we can witness theoretical and implementation details that make NODEO depart slightly from the original LDDMM formulation.

The purpose of our work is to close up NODEO original formulation to LDDMM by including LDDMM original regularizer into the loss function and embedding some theoretical justifications into the LDDMM theory. In addition, we provide a successful approximation of two variants of PDE-LDDMM [26] with NODEs. Table 3 in the Appendix shows a diagram of the methodological landscape of our work. With respect to the original NODEO, our proposed methods show an improved compromise between accuracy and transformation smoothness. In addition, our proposed methods greatly outperform their traditional counterparts and the most popular deep-learning approaches yielding diffeomorphic or nearly diffeomorphic solutions.

Our manuscript proceeds as follows. Section 2 provides an overview of the theory behind LDDMM and presents our extension to NODEO-LDDMM. Section 3 revisits the most relevant PDE-LDDMM methods and presents our two NODEO-PDE-LDDMM variants. Section 4 shows the evaluation study conducted with our proposed methods. Finally, Section 5 gathers the most relevant conclusions from our work.

2. LDDMM and NODEO-LDDMM formulations

2.1. LDDMM

Let I_0 and I_1 be the moving (source) and fixed (target) images representing the input of the image registration problem. In the continuous domain, the images are represented by square-integrable functions $I_i : \Omega \rightarrow \mathbb{R}$, where Ω is a rectangular domain in $\mathbb{R}^d$. For volumetric images, $d = 3$. $Diff(\Omega)$ represents the Riemannian manifold of smooth diffeomorphisms on Ω. V is the tangent space of the Riemannian structure at the identity diffeomorphism, id. V is a space of smooth vector fields on Ω. $Diff(\Omega)$ has a Lie group structure, and V is the corresponding Lie algebra.

Large Deformation Diffeomorphic Metric Mapping (LDDMM) was proposed by Beg et al. in 2005 [5]. The LDDMM problem is approached with a variational formulation from the minimization of the energy functional

$$E(v) = E_{\text{reg}}(v) + \frac{1}{\sigma^2} E_{\text{img}}(I_0 \circ \varphi^{-1}, I_1), \tag{1}$$

where $\varphi^{-1} : \Omega \rightarrow \mathbb{R}^d$ is the diffeomorphic transformation that warps the moving I_0 into the fixed I_1 image, the total energy E is decomposed into the regularization E_{reg} and the image similarity metric E_{img}, and $\frac{1}{\sigma^2}$ is the weight of the contribution of E_{reg} and E_{img} to E.

LDDMM assumes that transformations live in an appropriate Riemannian manifold of diffeomorphisms, $Diff(\Omega)$. The Riemannian metric of $Diff(\Omega)$ is defined from the scalar product in V

$$\langle v, w \rangle_V = \langle Lv, Lw \rangle_{L^2} = \langle L^\dagger L v, w \rangle_{L^2} = \int_\Omega \langle L^\dagger L v(x), w(x) \rangle d\Omega, \tag{2}$$

where $L = (Id - \alpha\Delta)^s$, $\alpha > 0$, $s \in \mathbb{R}$ is the invertible self-adjoint differential operator associated with the differential structure of $Diff(\Omega)$. The metric is right-invariant with respect to the composition of diffeomorphisms. V is a Reproducing Kernel Hilbert Space (RKHS) of vector fields.

Instead of defining the energy directly on φ^{-1}, the variational problem is parametrized by $v_t \in L^2([0,1], V)$, where v_t is a time-varying velocity field that represents the tangent vectors along the path of diffeomorphisms ϕ_t with beginning in the identity $\phi_0 = id$ and end in $\phi_1 = \varphi$, yielding the minimum energy solution for the LDDMM problem. The transport equation

$$\frac{d\phi_t}{dt} = v_t \circ \phi_t \tag{3}$$

corresponds with the Riemannian exponential map between the elements in V and the corresponding elements in the manifold of diffeomorphisms $Diff(\Omega)$. The inverse exponential map between the elements in $Diff(\Omega)$ and V is the Riemannian logarithm. In $Diff(\Omega)$, computing or approximating the logarithm is notably challenging due to the complexity of the manifold structure and the nonlinearity of the problem.

In LDDMM, the regularization energy is defined from

$$E_{\text{reg}}(v) = \int_0^1 \|v_t\|_V^2 \, dt, \tag{4}$$

where $\|\cdot\|_V^2 = \langle \cdot, \cdot \rangle_V$. Thus, the length of the path of diffeomorphisms ϕ_t is given by $E_{\text{reg}}(v)$. Under the exact matching assumption at convergence, $E_{\text{img}}(I_0 \circ \varphi^{-1}, I_1) = 0$ and the solution v_t yields a flow of diffeomorphisms ϕ_t which is a geodesic in $Diff(\Omega)$ with the Riemannian metric. This is the motivation below the word “metric” in LDDMM. In practice, the matching is not exact and the solutions depart slightly from belonging to geodesic paths.

The image similarity energy is defined from

$$E_{\text{img}}(I_0 \circ \varphi^{-1}, I_1) = \|I_0 \circ \varphi^{-1} - I_1\|_{L^2}^2, \tag{5}$$

although the energy minimization approach is amenable to the most commonly used image similarity metrics in medical image registration problems, such as normalized cross-correlation (NCC), its localized version (lNCC), mutual information (MI), and normalized gradient fields (NGF) [27–29].

Gradient-descent is used in the optimization process. The derivation of the gradient $\nabla_v E(v)$ is obtained from the Hilbert space structure of V and the relationship between Gâteaux derivatives and Fréchet differentials. Let the velocity field v be perturbed along the direction h. The Gâteaux variation is given by

$$\partial_h E(v) = \lim_{\tau \to 0} \frac{E(v + \tau h) - E(v)}{\tau} = \int_0^1 \langle \nabla_v E_t, h_t \rangle_V \, dt. \tag{6}$$

The derivation can be obtained from the Gâteaux variations of the regularization and the image similarity energies. The Gâteaux variation of the regularization is given by

$$\partial_h E_{\text{reg}}(v) = 2\int_0^1 \langle v_t, h_t \rangle_V \, dt. \tag{7}$$

The Gâteaux variation of the image similarity is given by

$$\partial_h E_{\text{img}}(v) = \frac{2}{\sigma^2}\int_0^1 \langle I_0 \circ \phi_{1,0} - I_1, DI_0 \circ \phi_{1,0} \; \partial_h \phi_{1,0} \rangle_{L^2} \, dt, \tag{8}$$

Using the notation trick $\phi_{s,t} = \phi_t \circ \phi_s^{-1}$, the diffeomorphism $\phi_{1,0} = \phi_0 \circ \phi_t^{-1} = \phi_t^{-1}$. From the integral expansion of $\partial_h \phi_{1,0}$ derived in [5] and the change of variables $\phi_{1,t}(x) = y$ we get

$$\partial_h E_{\text{img}}(v) = \int_0^1 \langle \nabla_v E_{\text{img}}, h_t \rangle_V \, dt, \tag{9}$$

where

$$\nabla_v E_{\text{img}}(v_t) = -\frac{2}{\sigma^2}(L^\dagger L)^{-1}\left(|D\phi_{t,1}|(I_0 \circ \phi_{t,0} - I_1)\nabla(I_0 \circ \phi_{t,0})\right). \tag{10}$$

Starting from $v_t = 0_V, t \in [0,1]$, the gradient-descent leads the optimization toward a local minimum in the direction of the energy gradient with the gradient-descent update equation

$$v_t^{n+1} = v_t^n - \epsilon \nabla_v E(v_t^n), \tag{11}$$

where

$$\nabla_v E(v_t) = 2v_t - \frac{2}{\sigma^2}(L^\dagger L)^{-1}\left(|D\phi_{t,1}|(I_0 \circ \phi_{t,0} - I_1)\nabla(I_0 \circ \phi_{t,0})\right). \tag{12}$$

While for gradient-descent the optimization is sensitive to the initial selection and refinement strategy of parameter ϵ, Gauss–Newton is typically able to converge to acceptable local minima with $\epsilon = 1.0$. In addition, the method shows a super-linear convergence rate, which increases the efficiency of the optimization despite the extra burden in the computation of the Hessian [16].

The time-varying parametrization of the velocity fields of the LDDMM problem was replaced with a constant in time parametrization using stationary or steady velocity fields [16]. Due to the computational efficiency, the stationary parametrization has been extensively adopted in modern deep-learning approaches [22,30–32].

2.2. NODEO-LDDMM

NODEO stands for Neural Ordinary Differential Equation Optimization. The method was proposed in [23] as a fresh learning-based approach to the non-rigid registration problem using Neural Ordinary Differential Equations (NODEs). NODEs were first proposed in [24] as a learning-based approach to ODE solvers. The method is inspired by the analogies between the Euler method and ResNet [33] and replaces the residual network itself with a function leading the depth of the neural network from discrete to infinite dimension thus leveraging the accuracy of the solvers. We proceed to describe the formulation of our proposed NODEO-LDDMM and discuss the differences with respect to NODEO-CVPR22.

Given an ODE in the shape of

$$\frac{dy}{dt} = f(y(t), t), \tag{13}$$

with initial condition $y(t_0) = y_0$, neural ODEs aim at learning the function f parametrized by θ in the shape of a neural network. Thus, the objective is to learn f_θ from

$$\frac{dz}{dt} = f_\theta(z(t), t) \tag{14}$$

where

$$z(t) = z_0 + \int_{t_0}^{t_1} f_\theta(z(t), t), \tag{15}$$

and

$$\mathcal{L}(z(t_1)) = \mathcal{L}\left(z_0 + \int_{t_0}^{t_1} f_\theta(z(t), t)dt\right) \tag{16}$$

is used as a loss function.

NODEO-LDDMM approaches the ODE solver of the original LDDMM problem with NODEs. Thus, the solution of the transport equation is estimated by the NODEs

$$\frac{d\phi_{0,t}}{dt} = v_t^\theta(\phi_{0,t}), \tag{17}$$

where, similarly to Eq. (15),

$$\phi_{0,s} = \phi_{0,0} + \int_0^s v_t^\theta(\phi_{0,t})dt. \tag{18}$$

Notice the correct analogies between the transport equation in [5] and Eq. (17). The approach also allows computing the solution $\phi_{t,0}$ of the transport equation

$$\frac{d\phi_{t,0}}{dt} = -v_t^\theta(\phi_{t,0}), \text{ where } \phi_{s,0} = \phi_{0,0} + \int_0^s -v_t^\theta(\phi_{t,0})dt, \tag{19}$$

yielding φ^{-1} at time 1, and also learn a function representation of the right-hand-side of the transport equation $-v_t \circ \phi_{t,0}$ through a neural network $-v_t^\theta(\phi_{t,0})$.

The loss function in NODEO-LDDMM is

$$\mathcal{L}(I_0, I_1, v_t^\theta(\phi_{t,0})) = \mathcal{L}_{\text{reg}}(v_t^\theta(\phi_{t,0})) + \mathcal{L}_{\text{sim}}\left(I_0, I_1, \phi_{0,0} + \int_0^1 -v_t^\theta(\phi_{t,0})dt\right). \tag{20}$$

The image similarity in $\mathcal{L}_{\text{sim}}$ is lNCC while the regularization $\mathcal{L}_{\text{reg}}$ is borrowed from previous proposals [22,23,30,34]

$$\mathcal{L}_{\text{reg}} = \lambda_{\text{lddmm}}\mathcal{L}_{\text{lddmm}} + \lambda_{\text{grad}}\mathcal{L}_{\text{grad}} + \lambda_{\text{Jdet}}\mathcal{L}_{\text{Jdet}}, \tag{21}$$

where

$$\mathcal{L}_{\text{lddmm}} = \int_0^1 \|v_t^\theta(\phi_{t,0})\|_V^2 \, dt,$$

$$\mathcal{L}_{\text{grad}} = \|\nabla\phi_{1,0}\|_{L^2}^2, \text{ and}$$

$$\mathcal{L}_{\text{Jdet}} = \int_\Omega (\max(0, -J_{\phi_{1,0}}(x) + \epsilon))^2 d\Omega, \tag{22}$$

where $\epsilon < 1$.

It should be noticed that the regularization in LDDMM is imposed on v_t while in NODEO-LDDMM the regularization $\mathcal{L}_{\text{lddmm}}$ is imposed on $-v_t^\theta(\phi_{t,0})$ which is a neural network representation of the right-hand-side $-v_t \circ \phi_{t,0}$. Expanding the $\mathcal{L}_{\text{lddmm}}$ expression and applying the change of variable $\phi_{t,0}(x) = y$ we get

$$\mathcal{L}_{\text{lddmm}} = \int_0^1 \langle v_t^\theta \circ \phi_{t,0}(x), v_t^\theta \circ \phi_{t,0}(x) \rangle_V \, dx dt = \int_0^1 |D\phi_{0,t}(y)| \langle v_t^\theta(y), v_t^\theta(y) \rangle_V \, dy dt. \tag{23}$$

In the case that $|D\phi_{0,t}(y)| > 1$ and for the same regularization energy or loss, the norm $\|v_t^\theta(y)\|_V^2$ in NODEO-LDDMM would be smaller than in LDDMM, leading to less deformation for $\phi_{t,0}$. Conversely, if $|D\phi_{0,t}(y)| < 1$, the norm in NODEO-LDDMM would be larger than LDDMM, resulting in more deformation for $\phi_{t,0}$. The regularization in NODEO-LDDMM needs to be applied to $-v_t^\theta(\phi_{t,0})$ and we need to accept the subtle difference between LDDMM and NODEO-LDDMM regularization and the effect in the amount of deformation.

Regarding the Jacobian loss, $\mathcal{L}_{\text{Jdet}}$, the case of $J_{\phi_{1,0}}(x) \geq \epsilon$ holds $\mathcal{L}_{\text{Jdet}} = 0$. For Jacobian values ranging from ϵ to negative values, the Jacobian loss increases proportionately. Therefore, the Jacobian loss promotes convergence towards models in which the diffeomorphism $\phi_{1,0}$ should exhibit more controlled contractions while avoiding foldings.

Training is conducted for each registration pair. Starting from a random initialization of $-v_t^\theta(\phi_{t,0})$, forward and backward propagation iteratively improve the estimation of the network parameters θ according to the minimization of the loss function given in Eq. (20). This is a main difference between NODEO-LDDMM and other deep-learning approaches so far like VoxelMorph [22], SymNet [30], LapIRN [31], SynthMorph [35], or TransMorph [32].

2.3. NODEO-LDDMM vs. NODEO-CVPR22

The main differences between NODEO-LDDMM and NODEO-CVPR22 involve the use of the LDDMM regularizer E_{reg} as a loss function $\mathcal{L}_{\text{lddmm}}$. In addition, the authors claim the need to apply a Gaussian kernel in the last layer of the CNN architecture and they use the term Kv_t^θ in Eqs. (19), (20), and (22). Based on empirical observations, this could be attributed to NODEO-CVPR22 architecture without K not being sufficiently capable of learning smooth models from the regularization losses. Assuming that the Gaussian kernel is the RKHS operator of the transformation model, then the variable v_t^θ would actually represent the momentum of the velocity field and the network parameters would be adjusted to learn the momentum, not the velocity field. A more elegant explanation is that auto gradient is computing the gradient of the loss function in the space of L^2 functions, however, the gradient needs to be computed in V [5]. Then, the use of a Gaussian kernel in the last layer of the CNN architecture is a transformation of the L^2 differentials into V differentials considering a Gaussian RKHS structure of V. Therefore, NODEO-LDDMM provides a formulation for the problem more consistent with LDDMM theory.

Analyzing the codes available in the GIT repository https://github.com/yifannnwu/NODEO-DIR, two remarkable implementation details come to light. First of all, the authors used a stationary parametrization for the NODES. This means that v_t^θ does not depend on time and the authors are solving the problem for the stationary parametrization. Second, the computation of the inverse of the exponential mapping

$$\log : Diff(\Omega) \to V,\ \phi_t \to v_t, \tag{24}$$

is needed for the computation of the regularization loss. This is circumvented with the rough approximation

$$v_t \approx \phi_{t+1} - \phi_t \tag{25}$$

that introduces an intrinsic error in the solutions. With NODEO-LDDMM we propose to use the result of the forward pass of the neural network.

To establish a fair comparison between both methodologies, we used the same CNN architecture as in NODEO-CVPR22 (replacing K operator with $(L^\dagger L)^{-1}$). In future work, we will explore the effect of non-stationary NODE solvers, time-dependent CNNs, and other model architectures such as transformers [36] or Multi Layer Perceptrons (MLP), widely used in implicit representations [37–39].

3. PDE-LDDMM and NODEO-PDE-LDDMM formulations

PDE-LDDMM consists of a formulation analytically but not numerically equivalent to Beg et al. LDDMM using an optimal control approach [11,12]. The fundamental constraints in PDE-LDDMM are derived from the inverse consistency identity, $\phi_{0,t} \circ \phi_{0,t}^{-1} = id$, that, together with the transport equation yield the deformation state equation

$$\partial_t \phi_{t,0} + D\phi_{t,0} \cdot v_t = 0 \tag{26}$$

with initial condition $\phi_0 = id$ [5]. Depending on the desired model of constrained deformations, alternative equations can be incorporated to the constrained variational formulation such as the incompressibility constraint [13] or the EPDiff equation [40], among others.

3.1. PDE-LDDMM based on the image state equation

The original PDE-LDDMM method proposed by Hart et al. in [11] approached the LDDMM problem with a constrained variational formulation where the constraint was based on the restriction of the deformation state equation from maps to images. Let $m(t)$ represent the warped images $I_0 \circ \phi_{t,0}$. Thus, the problem is defined from the minimization problem

$$E(v) = \int_0^1 \|v_t\|_V^2 dt + \frac{1}{\sigma^2} \|m(1) - I_1\|_{L^2}^2 \tag{27}$$

subject to

$$\partial_t m_t + \nabla m_t \cdot v_t = 0 \tag{28}$$

with initial condition $m(0) = I_0$ (see the analogy with Eq. (26)). The differentiation of the augmented Lagrangian with respect to the state variable m and its adjoint variable λ yield the optimality conditions

$$\begin{aligned} \partial_t m_t + \nabla m_t \cdot v_t = 0, m(0) = I_0 \text{ (forward)} \\ -\partial_t \lambda_t - \nabla \cdot (\lambda_t \cdot v_t) = 0, \lambda(1) = \frac{2}{\sigma^2}(I_1 - m(1)) \text{ (backward)}, \end{aligned} \tag{29}$$

and the gradient (in L^2) needed for gradient-descent optimization

$$\nabla_{L^2} E(v) = 2L^\dagger Lv + \lambda \nabla m. \tag{30}$$

From the optimal control point of view, v is the control, m is the state, and λ is the adjoint variable. The objective of the PDE-LDDMM approach was to avoid the expensive computations in the deformation space by the translation of the computations to the image space through the solution of the image state equation.

3.2. PDE-LDDMM based on the deformation state equation

Inspired by the previous PDE-LDDMM contributions, Hernandez successfully explored the idea of obtaining more stability and accuracy by relying on the deformation state equation [26,40,41]. The author proposed two different methods, one using the expressions of the state and adjoint variables that can be derived from the equivalence between Hart et al. PDE-LDDMM [11] and original LDDMM [5]. The second one directly imposed the deformation state equation as a constraint.

Thus, the first method (PDE-LDDMM$_{\text{st eq}}$) uses the deformation state equation (Eq. (26)) for the computation of the forward and inverse paths, $\phi_{t,0}$ and $\phi_{0,t}$,

$$\begin{aligned} \partial_t \phi_{t,0} + D\phi_{t,0} \cdot v_t = 0, \phi_{0,0} = id \text{ (forward)} \\ -\partial_t \phi_{0,t} - D\phi_{0,t} \cdot v_t = 0, \phi_{0,1} = id \text{ (backward)}, \end{aligned} \tag{31}$$

and then it uses the expressions

$$\begin{aligned} J_t &= |D\phi_{0,t}| \\ m(t) &= I_0 \circ \phi_{t,0} \\ \lambda(t) &= J_t \lambda(1) \circ \phi_{0,t} \end{aligned} \tag{32}$$

in the computation of the gradient $\nabla_{L^2} E(v)$ from Eq. (30).

The second method (PDE-LDDMM$_{\text{def eq}}$) solves Eq. (27) subject to the forward equation in Eq. (31). The differentiation of the augmented Lagrangian with respect to the state variable ϕ and its adjoint variable ρ yield the optimality conditions

$$\begin{aligned} \partial_t \phi_{t,0} + D\phi_{t,0} \cdot v_t = 0, \phi_{0,0} = id \text{ (forward)} \\ -\partial_t \rho_t - \nabla \cdot (\rho_t \cdot v_t) = 0, \rho(1) = \lambda(1) \cdot \nabla m(1) \text{ (backward)}, \end{aligned} \tag{33}$$

and the gradient needed for gradient-descent optimization is, in this case,

$$\nabla_{L^2} E(v) = 2L^\dagger Lv + D\phi \cdot \rho. \tag{34}$$

Originally, Runge–Kutta was used for the computation of the solutions of the ODEs. The equations for Semi-Lagrangian integration were derived in [41]. They improved the stability of the solvers while reducing the complexity with the number of time steps. Both methods outperformed PDE-LDDMM based on the image state equation (the method in Section 3.1).

3.3. NODEO-PDE-LDDMM

We propose to depart from traditional PDE-LDDMM approaching the ODE solvers of the equations in PDE-LDDMM$_{\text{st eq}}$ and PDE-LDDMM$_{\text{def eq}}$ with their corresponding NODEs. Thus, in NODEO-PDE-LDDMM$_{\text{st eq}}$ we compute the solutions $\phi_{t,0}$ and $\phi_{0,t}$ (Eqs. (31)) using a forward and a backward NODE, respectively. Then, the variables J_t, $m(t)$, and $\lambda(t)$ are computed from Eq. (32) using the

Table 1

Baseline methods, NODEO-LDDMM and NODEO-PDE-LDDMM. Quantitative results on NIREP and OASIS-L2R22. Mean and standard deviation of the Dice Similarity Coefficient (DSC), maximum and minimum of the Jacobian determinant, number and percentage of negative Jacobian determinants, and standard deviation of the logarithm of the Jacobian determinant for those points with positive values. The arrows indicate that high DSC values while not extreme Jacobian determinant values are preferable. Boldface indicate, for each family of methods, the one with the best compromise between DSC average and minimum Jacobians ≥ −0.10, which is a reasonable threshold for nearly diffeomorphic solutions. For NODEO methods, the value of the regularization parameter α is indicated.

NIREP					
Method	DSC (%) ↑	max (J) ↓	min (J) ↑	# of $\lvert J_\phi \rvert \leq 0$ ↓	SDlogJ ↓
Affine	43.56 ± 1.94	–	–	–	–
VM-GIT 2021	**61.35 ± 2.24**	12.48 ± 2.17	**0.04 ± 0.06**	6 (< 0.01%)	0.28 ± 0.01
SyMNet-Diff	**61.13 ± 2.24**	15.27 ± 2.25	**−0.15 ± 0.27**	29 (< 0.01%)	0.31 ± 0.01
LapIRN-Diff	60.44 ± 1.23	6.66 ± 0.78	0.16 ± 0.03	0	0.22 ± 0.01
TransMorph-BSpl IXI	58.95 ± 1.69	10.63 ± 1.90	0.06 ± 0.02	0	0.28 ± 0.00
ANTS	60.24 ± 1.35	4.11 ± 0.39	0.24 ± 0.03	0	0.15 ± 0.00
StLDDMM	**62.10 ± 1.54**	15.09 ± 4.46	**0.02 ± 0.22**	39 (< 0.01%)	0.27 ± 0.01
PDE-LDDMM$_{st\ eq}$	60.11 ± 2.81	7.41 ± 3.56	0.01 ± 0.01	0	0.23 ± 0.02
PDE-LDDMM$_{def\ eq}$	60.92 ± 1.88	15.59 ± 5.89	0.05 ± 0.03	0	0.24 ± 0.03
NODEO-CVPR22	63.74 ± 0.90	11.02 ± 2.69	−0.19 ± 0.12	776 (0.014%)	0.28 ± 0.01
NODEO-LDDMM 0.0001	65.25 ± 1.52	13.17 ± 3.26	−0.78 ± 0.37	4157 (0.077%)	0.31 ± 0.02
NODEO-LDDMM 0.00025	64.39 ± 1.50	11.22 ± 3.07	−0.29 ± 0.23	1383 (0.025%)	0.29 ± 0.02
NODEO-LDDMM 0.0005	**62.83 ± 1.25**	8.93 ± 1.50	**−0.06 ± 0.12**	242 (< 0.01%)	0.28 ± 0.01
NODEO-LDDMM 0.0010	60.01 ± 1.83	6.64 ± 1.09	0.10 ± 0.12	1 (< 0.01%)	0.26 ± 0.02
NODEO-PDE-LDDMM$_{st\ eq}$ 0.0001	65.26 ± 1.73	14.02 ± 2.86	−0.65 ± 0.34	4243 (0.079%)	0.31 ± 0.02
NODEO-PDE-LDDMM$_{st\ eq}$ 0.00025	63.95 ± 1.78	10.91 ± 3.27	−0.30 ± 0.32	1077 (0.022%)	0.27 ± 0.02
NODEO-PDE-LDDMM$_{st\ eq}$ 0.0005	**62.64 ± 1.32**	8.55 ± 1.41	**−0.01 ± 0.07**	100 (< 0.01%)	0.27 ± 0.00
NODEO-PDE-LDDMM$_{st\ eq}$ 0.0010	60.21 ± 1.72	6.54 ± 0.98	0.09 ± 0.07	10 (< 0.01%)	0.27 ± 0.00
NODEO-PDE-LDDMM$_{def\ eq}$ 0.0001	63.81 ± 5.82	11.67 ± 3.89	−0.50 ± 0.47	3304 (0.061%)	0.28 ± 0.07
NODEO-PDE-LDDMM$_{def\ eq}$ 0.00025	64.28 ± 1.75	10.88 ± 2.56	−0.26 ± 0.12	1101 (0.020%)	0.28 ± 0.01
NODEO-PDE-LDDMM$_{def\ eq}$ 0.0005	**62.75 ± 1.46**	9.63 ± 3.07	**−0.06 ± 0.08**	236 (< 0.01%)	0.27 ± 0.00
NODEO-PDE-LDDMM$_{def\ eq}$ 0.0010	60.25 ± 1.40	6.53 ± 0.85	0.09 ± 0.05	1 (< 0.01%)	0.26 ± 0.00
OASIS-L2R22 validation set					
Method	DSC (%) ↑	max (J) ↓	min (J) ↑	# of $\lvert J_\phi \rvert \leq 0$ ↓	SDlogJ ↓
Affine	57.18 ± 5.17	–	–	–	–
VM-GIT 2021	75.25 ± 3.77	26.61 ± 11.66	0.03 ± 0.02	4 (< 0.01%)	0.32 ± 0.04
SyMNet-Diff	77.78 ± 2.66	18.82 ± 3.78	−0.11 ± 0.24	30 (< 0.01%)	0.34 ± 0.01
LapIRN-Diff	77.03 ± 3.18	4.56 ± 1.25	0.24 ± 0.05	0	0.15 ± 0.01
TransMorph-BSpl IXI	**77.04 ± 2.54**	14.65 ± 4.59	**−0.09 ± 0.18**	105 (< 0.01%)	0.32 ± 0.01
ANTS	77.07 ± 3.49	4.36 ± 0.67	0.23 ± 0.04	0	0.18 ± 0.01
StLDDMM	77.47 ± 2.81	32.16 ± 70.55	−0.52 ± 1.05	2976 (0.051%)	0.30 ± 0.05
PDE-LDDMM$_{st\ eq}$	73.30 ± 5.32	11.51 ± 6.83	0.00 ± 0.01	0	0.26 ± 0.04
PDE-LDDMM$_{def\ eq}$	**76.12 ± 2.61**	47.39 ± 80.02	**0.08 ± 0.03**	0	0.22 ± 0.02
NODEO-CVPR22	79.20 ± 2.56	18.43 ± 5.40	−0.43 ± 0.22	7438 (0.129%)	0.41 ± 0.03
NODEO-LDDMM 0.0001	80.37 ± 2.70	29.74 ± 13.42	−1.30 ± 0.54	25 320 (0.440%)	0.50 ± 0.06
NODEO-LDDMM 0.00025	79.76 ± 2.55	22.51 ± 7.39	−0.62 ± 0.24	11 402 (0.198%)	0.43 ± 0.04
NODEO-LDDMM 0.0005	78.96 ± 2.44	16.65 ± 8.81	−0.26 ± 0.15	3705 (0.064%)	0.38 ± 0.03
NODEO-LDDMM 0.0010	**77.45 ± 2.43**	11.38 ± 5.87	**−0.04 ± 0.08**	1062 (0.018%)	0.35 ± 0.02
NODEO-LDDMM 0.0015	75.01 ± 4.76	7.33 ± 3.02	0.09 ± 0.24	537 (< 0.01%)	0.31 ± 0.08
NODEO-LDDMM 0.0025	74.60 ± 2.80	5.76 ± 1.98	0.10 ± 0.08	266 (< 0.01%)	0.32 ± 0.02
NODEO-PDE-LDDMM$_{st\ eq}$ 0.0001	80.37 ± 2.63	28.98 ± 10.17	−1.18 ± 0.25	26 310 (0.458%)	0.50 ± 0.05
NODEO-PDE-LDDMM$_{st\ eq}$ 0.00025	79.74 ± 2.52	23.89 ± 10.61	−0.66 ± 0.30	10 532 (0.183%)	0.42 ± 0.03
NODEO-PDE-LDDMM$_{st\ eq}$ 0.0005	78.87 ± 2.35	15.44 ± 5.55	−0.21 ± 0.11	2975 (0.051%)	0.37 ± 0.02
NODEO-PDE-LDDMM$_{st\ eq}$ 0.0010	**77.24 ± 2.55**	10.81 ± 5.39	**−0.04 ± 0.06**	990 (0.017%)	0.34 ± 0.02
NODEO-PDE-LDDMM$_{st\ eq}$ 0.0015	76.22 ± 2.74	8.38 ± 4.21	0.01 ± 0.08	811 (0.014%)	0.34 ± 0.03
NODEO-PDE-LDDMM$_{st\ eq}$ 0.0025	74.18 ± 3.04	5.82 ± 2.12	0.11 ± 0.08	0	0.31 ± 0.02
NODEO-PDE-LDDMM$_{def\ eq}$ 0.0001	80.33 ± 2.59	30.75 ± 16.60	−1.25 ± 0.28	25 471 (0.443%)	0.50 ± 0.04
NODEO-PDE-LDDMM$_{def\ eq}$ 0.00025	79.88 ± 2.47	23.67 ± 11.06	−0.55 ± 0.21	10 178 (0.177%)	0.42 ± 0.03
NODEO-PDE-LDDMM$_{def\ eq}$ 0.0005	78.77 ± 2.64	16.18 ± 8.17	−0.27 ± 0.21	3479 (0.060)	0.37 ± 0.03
NODEO-PDE-LDDMM$_{def\ eq}$ 0.0010	**77.38 ± 2.43**	10.60 ± 4.79	**−0.01 ± 0.06**	629 (0.010%)	0.34 ± 0.02
NODEO-PDE-LDDMM$_{def\ eq}$ 0.0015	76.17 ± 2.66	8.09 ± 3.34	0.03 ± 0.09	573 (0.011%)	0.33 ± 0.03
NODEO-PDE-LDDMM$_{def\ eq}$ 0.0025	73.12 ± 6.38	5.76 ± 2.55	0.16 ± 0.21	3 (< 0.01%)	0.30 ± 0.07
OASIS-L2R22 test set					
Method	DSC (%) ↑	max (J) ↓	min (J) ↑	# of $\lvert J_\phi \rvert \leq 0$ ↓	SDlogJ ↓
Affine	58.61 ± 5.09	–	–	–	–
VM-GIT 2021	77.66 ± 2.93	23.69 ± 9.58	0.00 ± 0.13	2 (< 0.01%)	0.28 ± 0.03
SyMNet-Diff	**78.71 ± 2.57**	21.74 ± 7.15	**−0.10 ± 0.20**	53 (< 0.01%)	0.34 ± 0.02
LapIRN-Diff	78.45 ± 2.23	4.52 ± 1.12	0.23 ± 0.05	0	0.16 ± 0.01
TransMorph-BSpl IXI	77.78 ± 1.49	13.13 ± 2.87	−0.05 ± 0.10	199 (< 0.01%)	0.32 ± 0.01

(*continued on next page*)

Table 1 (*continued*).

ANTS	79.21 ± 1.89	4.65 ± 1.07	0.22 ± 0.04	0	0.19 ± 0.02
StLDDMM	78.49 ± 1.77	16.55 ± 17.86	−0.35 ± 0.83	3480 (0.06%)	0.29 ± 0.04
PDE-LDDMM$_{\text{st eq}}$	75.98 ± 2.67	13.82 ± 15.70	0.01 ± 0.01	0	0.28 ± 0.03
PDE-LDDMM$_{\text{def eq}}$	**76.30 ± 2.36**	18.25 ± 17.67	**0.09 ± 0.04**	0	0.26 ± 0.02
NODEO-CVPR22	79.96 ± 1.52	18.47 ± 6.24	−0.46 ± 0.21	16 927 (0.29%)	0.42 ± 0.04
NODEO-LDDMM 0.0001	80.91 ± 1.66	29.11 ± 12.21	−1.37 ± 0.62	50 964 (0.89%)	0.50 ± 0.08
NODEO-LDDMM 0.00025	80.38 ± 1.61	19.54 ± 8.05	−0.63 ± 0.31	20 106 (0.35%)	0.42 ± 0.04
NODEO-LDDMM 0.0005	79.43 ± 1.59	14.63 ± 7.67	−0.22 ± 0.14	5944 (0.10%)	0.37 ± 0.04
NODEO-LDDMM 0.0010	**78.03 ± 1.59**	9.66 ± 4.34	**−0.03 ± 0.10**	2036 (0.04%)	0.35 ± 0.03
NODEO-LDDMM 0.0015	76.49 ± 2.67	7.34 ± 2.71	0.09 ± 0.16	1046 (0.02%)	0.32 ± 0.06
NODEO-LDDMM 0.0025	75.10 ± 3.70	5.65 ± 1.86	0.14 ± 0.15	831 (0.01%)	0.31 ± 0.06
NODEO-PDE-LDDMM$_{\text{st eq}}$ 0.0001	80.20 ± 4.98	28.67 ± 14.07	−1.27 ± 0.77	49 395 (0.86%)	0.49 ± 0.11
NODEO-PDE-LDDMM$_{\text{st eq}}$ 0.00025	80.39 ± 1.61	19.42 ± 8.61	−0.61 ± 0.26	20 668 (0.36%)	0.43 ± 0.05
NODEO-PDE-LDDMM$_{\text{st eq}}$ 0.0005	79.49 ± 1.57	14.56 ± 7.52	−0.21 ± 0.12	6716 (0.12%)	0.37 ± 0.04
NODEO-PDE-LDDMM$_{\text{st eq}}$ 0.0010	**78.01 ± 1.63**	9.59 ± 4.09	**−0.03 ± 0.09**	2051 (0.04%)	0.35 ± 0.04
NODEO-PDE-LDDMM$_{\text{st eq}}$ 0.0015	76.73 ± 1.89	7.60 ± 3.37	0.06 ± 0.09	1073 (0.02%)	0.33 ± 0.03
NODEO-PDE-LDDMM$_{\text{st eq}}$ 0.0025	75.00 ± 3.72	5.66 ± 2.08	0.15 ± 0.15	723 (0.01%)	0.31 ± 0.06
NODEO-PDE-LDDMM$_{\text{def eq}}$ 0.0001	81.00 ± 1.62	29.22 ± 12.65	−1.40 ± 0.56	55 729 (0.97%)	0.52 ± 0.08
NODEO-PDE-LDDMM$_{\text{def eq}}$ 0.00025	80.44 ± 1.54	19.80 ± 7.48	−0.62 ± 0.26	23 249 (0.40%)	0.43 ± 0.05
NODEO-PDE-LDDMM$_{\text{def eq}}$ 0.0005	79.47 ± 1.52	14.38 ± 6.34	−0.24 ± 0.12	7489 (0.13%)	0.38 ± 0.04
NODEO-PDE-LDDMM$_{\text{def eq}}$ 0.0010	**77.81 ± 1.80**	9.40 ± 3.57	**−0.02 ± 0.10**	1994 (0.03%)	0.34 ± 0.04
NODEO-PDE-LDDMM$_{\text{def eq}}$ 0.0015	76.42 ± 2.70	7.47 ± 3.04	0.08 ± 0.17	902 (0.02%)	0.32 ± 0.06
NODEO-PDE-LDDMM$_{\text{def eq}}$ 0.0025	75.58 ± 1.82	5.84 ± 1.69	0.12 ± 0.07	643 (0.01%)	0.32 ± 0.03

Table 2
NIREP16. Computation time and maximum VRAM memory usage achieved by the registration methods considered in our study. NODEO values are given for 300 iterations.

Method	Metric	Model	$time_{GPU}$ (s)	Peak VRAM (MBs)
VM-GIT 2021	SSD	`vxm_dense_brain_T1_3D_mse`	8.05	3739
SyMNet-Diff	lNCC	`SyMNet_smo30_update_80 000`	4.09	2888
LapIRN-Diff	lNCC	`LapIRN_diff_fea7`	3.16	5934
TransMorph-BSpl IXI	lNCC	`TransMorph_bspl_Validation_dsc0.750`	19.29	2772
ANTS[a]	lNCC	SyM-LDDMM	2065.24	2656
StLDDMM	lNCC	LDDMM	30.42	2733
PDE-LDDMM$_{\text{st eq}}$	lNCC	State equation	183.89	6159
PDE-LDDMM$_{\text{def eq}}$	NCC	Deformation equation	250.39	5899
NODEO-CVPR22	lNCC	Transport equation	76.10	5855
NODEO-LDDMM	lNCC	Transport equation	68.99	6029
NODEO-PDE-LDDMM$_{\text{st eq}}$	lNCC	State equation	252.35	11 999
NODEO-PDE-LDDMM$_{\text{st eq}}$	lNCC	Deformation equation	145.99	9233

[a] In ANTS indicates that the computation is performed in the CPU and RAM.

solutions $\phi_{t,0}$ and $\phi_{0,t}$. The expression for v_t is computed from the approximation

$$v \to -\frac{1}{2}(L^\dagger L)^{-1}(\lambda \nabla m) \tag{35}$$

previously used in the LDDMM literature [42]. This approximation comes from the fact that, during optimization, $\nabla_{L^2} E(v) \to 0$, and then the right-hand-side of Eq. (30) can be considered a rough approximation of v at the beginning of the optimization process that increases its precision iteratively. Finally, the losses analogous to NODEO-LDDMM are computed, backward propagation is performed, and the parameters of the forward and backward NODEs are updated.

In PDE-LDDMM$_{\text{def eq}}$ we compute the solutions of $\phi_{t,0}$ and ρ_t in Eq. (33) using a forward and a backward NODE, respectively. Notice that $\phi_{t,0}$ is represented with a vector field while ρ_t is represented with a scalar field. Therefore, the network architectures and the forward passes of the networks are different. Then, the expression for v_t is computed from the approximation

$$v \to -\frac{1}{2}(L^\dagger L)^{-1}(D\phi \cdot \rho). \tag{36}$$

The same reasoning as in Eq. (35) holds for its justification, although, to our knowledge, this is the first time that it has been proposed. Finally, the losses analogous to NODEO-LDDMM are computed, backward propagation is performed, and the parameters of the forward and backward NODEs are updated.

Last but not least, our NODEO-PDE-LDDMM approach allows the computation of v_t directly from Eq. (35) or Eq. (36). Therefore, the problem raised with NODEO-LDDMM and the estimation of the logarithm map does not hold. The regularization loss $\mathcal{L}_{\text{lddmm}}$ is defined on v_t in agreement with LDDMM regularization. The regularization loss $\mathcal{L}_{\text{grad}}$ is also defined on $\nabla \phi_{1,0}$. As in NODEO original formulation, lNCC is selected as the image similarity metric.

4. Results

4.1. Datasets

We have evaluated our proposed methods in two different datasets extensively selected for the evaluation of non-rigid registration methods:

NIREP. The Non-rigid Image Registration Evaluation Project (NIREP) was proposed in [43] for the evaluation of non-rigid registration. NIREP consists of 16 T1 Magnetic Resonance Imaging (MRI) images. These images were acquired at the Human Neuroanatomy and Neuroimaging Laboratory, University of Iowa. They were selected for the NIREP project from a database of 240 normal volunteers. Datasets correspond to young 8 males and 8 females with a mean age of 32.5 ± 8.4 and 29.8 ± 5.8 years, respectively. The images are skull-stripped and aligned according to the anterior and posterior commissures. Images are distributed with the segmentation of 32 gray matter regions at the frontal, parietal, temporal, and occipital lobes. The most remarkable feature of this dataset is its excellent image quality. The geometry of the manual segmentations provides a specially challenging framework for

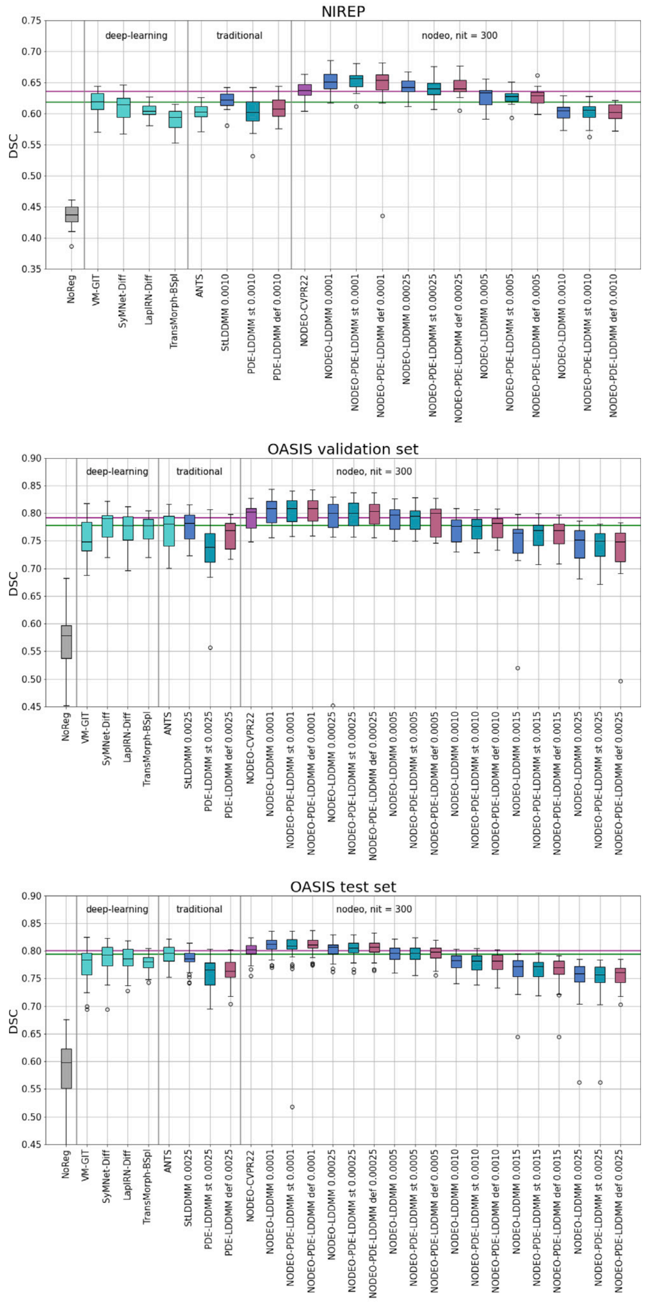

Fig. 1. Volume overlap obtained by the registration methods measured in terms of the Dice Similarity Coefficient (DSC) between the warped and the corresponding target segmentations. Box and whisker plots show the distribution of the DSC values averaged over the segmentations. The green line indicates the mean of the best benchmark method (VoxelMorph for NIREP, TransMorph for OASIS val and SyMNet for OASIS test) and the magenta line indicates the mean of NODEO-CVPR22, facilitating the comparisons.

deformable registration evaluation. In this work, a subsampled version of this dataset is used for the evaluation of the methods following the guidelines in [16]. The images are subsampled reducing image dimensions to 180 × 212 × 180. Subsampling is needed to be able to run interesting but memory-demanding benchmark methods and to maintain the continuity of the evaluation results shown in previous works [40,41,44]. In our experiments, the first image is selected as the source and warped to the remaining 15 images of the dataset.

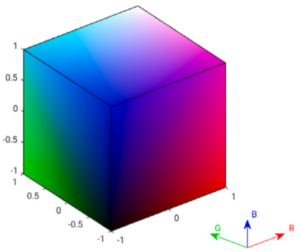

Fig. 2. RGB cube to facilitate the interpretation of the colormap used in the figures of the displacement fields. It should be noticed that the origin of coordinates is located at the center of the cube, therefore, displacements close to zero will be represented in gray.

OASIS-L2R22. The open-access series of imaging studies, OASIS (https://www.oasis-brains.org/), is a project aimed at making neuroimaging data sets of the brain freely available to the scientific community. OASIS is divided into different projects with a focus on the study of the anatomical evolution of normal and diseased brains. OASIS-L2R22 dataset is a small sample made of 416 3D T1 MRI scans from different subjects. The dataset was proposed in the Learn2Reg challenge with the intention to assess the performance of non-rigid registration methods in the alignment of small structures of variable shape and size from monomodal MRI [45]. There is no available information regarding the sex or the age of the subjects. The original OASIS images were pre-processed for the HyperMorph paper [46]. Preprocessing included resampling and alignment to a common template and skull stripping. The segmentations were automatically obtained using FreeSurfer and SAMSEG from the neurite package (https://surfer.nmr.mgh.harvard.edu/fswiki/Samseg). A total of 35 brain structures are customarily used in the evaluation. The registration pairs are given by the challenge organizers. The image dimensions are 160 × 224 × 192.

The validation set is made up of 19 image pairs while the test set is made up of 39 image pairs. The validation set can be used for the evaluation of non-rigid registration methods in the case that the data has not been involved in the model design. For the test set, the segmentations are not publicly available. To obtain the evaluation metrics of non-rigid registration methods in the test set, the methods should be implemented in Python and submitted to the challenge platform through a docker before the challenge deadline. This means rewriting the codes for traditional methods, typically built on C++ or Matlab. For our work, we segmented the test images using SAMSEG (accessed in March 2024). We observed that this version of SAMSEG provides much more labels than the Learn2Reg segmentations and there is a mismatch in the labels assigned to corresponding structures. We manually combined and reassigned the labels to be mostly in correspondence with the Learn2Reg segmentations. We validated the differences of our segmentations in the validation set, getting only slight differences with respect to Learn2Reg segmentations.

4.2. Benchmark methods

In this work, we selected the traditional LDDMM and PDE-LDDMM methods closest to our work as benchmark methods. In addition, we selected the most popular unsupervised deep-learning approaches with available source code and models trained in the T1 MRI registration problem, preferably with diffeomorphic variants. Since the number of different LDDMM and PDE-LDDMM variants is considerable, and given the prevalence of the stationary parametrization of diffeomorphisms in unsupervised deep-learning approaches, we focused our study on the evaluation of stationary variants. We selected as benchmark the best-performing stationary versions of LDDMM and PDE-LDDMM in [29] (NCC or lNCC image similarity and Gauss–Newton–Krylov optimization) and ANTS (lNCC image similarity) [47]. From the deep-learning

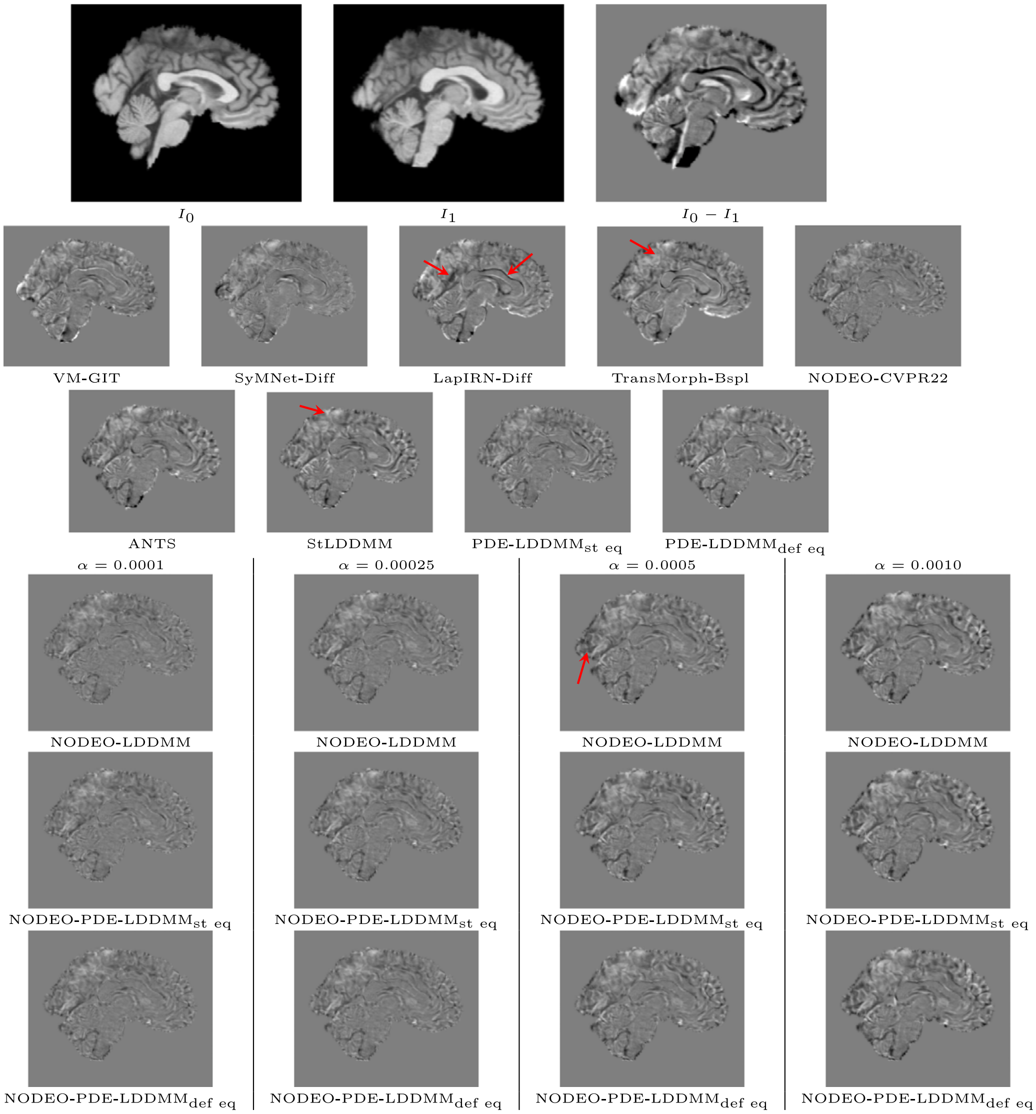

Fig. 3. NIREP. Sagittal view of the differences after registration $I_0 \circ \varphi^{-1} - I_1$ in a representative experiment. Red arrows point out (in order of appearance) the parieto-occipital sulcus, the corpus callosum, the parietal lobe, the central sulcus and the occipital lobe. These are the locations where the methods showed the most remarkable intensity differences.

methods we selected VoxelMorph [21], SyMNet [30], LapIRN [31] and the B-Spline version of TransMorph [32]. NODEO-CVPR22 with the default parameters was also selected as a benchmark [23].

4.3. Implementation details and parameters

The experiments were run on a machine equipped with one NVidia GeForce RTX 3090 Ti with 24 GBS of video memory and an Intel Core i7 with 64 GBS of DDR3 RAM. The C++ code of ANTS library was used for the SyN method. The LDDMM codes were developed in the GPU with Matlab. The Python codes available in the GIT repository https://github.com/yifannnwu/NODEO-DIR served as a basis for the implementation of our proposed methods.

For the traditional methods, we used the same implementation and parameters as in [29]. All methods were embedded into a multi-resolution scheme of three levels. Gauss–Newton and Gauss–Newton–Krylov were implemented with an efficient method for the update of the step size based on offline backtracking line-search combined with a check on Armijo's condition. We used the stopping conditions in [12]. Otherwise, the optimization was stopped after 50 iterations in the case of Gauss–Newton and after 5 inner × 10 outer iterations in the case of Gauss–Newton–Krylov.

Regularization parameters were selected from a search of the optimal parameters in NIREP16 and OASIS datasets. Thus, we used $\sigma^2 = 1.0$, $s = 2$, and a unit-domain discretization of the image domain Ω. The regularization parameter α was selected from a search of the optimal parameter value in NIREP and OASIS-L2R22 validation datasets. The details can be found in the Appendix.

ANTS was run with the following parameters
`synconvergence="[50x50x50,1e-6,10]"`,
`synshrinkfactors="4x2x1"`,
`synsmoothingsigmas="3x2x1vox"`.

The selection of the number of iterations was in agreement with the number of iterations used in Gauss–Newton and the number of inner × outer iterations used in Gauss–Newton–Krylov optimization for PDE-LDDMM. The selection of the Gaussian smoothing parameters resulted in a minimal regularization with the objective of obtaining a maximal image matching.

NODEO-CVPR22 was executed with the default parameters. The mean filter was used as smoothing kernel. The number of time steps was 2, yielding a stationary parametrization. The weighting parameters were $\lambda_{\mathrm{lddmm}} = 0.0005$, $\lambda_{\mathrm{grad}} = 0.05$, and $\lambda_{\mathrm{Jdet}} = 2.5$. The same parameters were used in NODEO-LDDMM and NODEO-PDE-LDDMM.

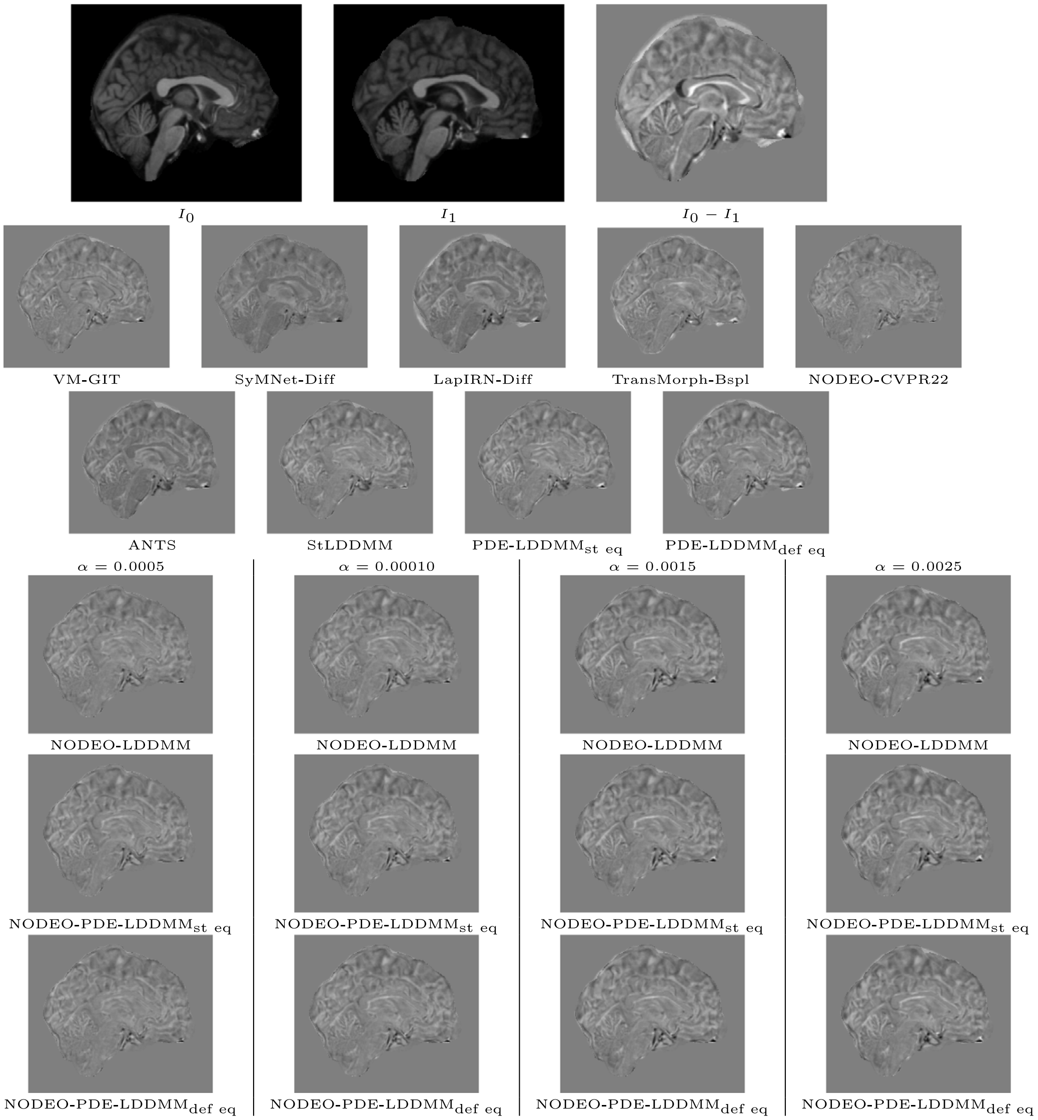

Fig. 4. OASIS-L2R22. Sagittal view of the differences after registration $I_0 \circ \varphi^{-1} - I_1$ in a representative experiment.

4.4. Evaluation metrics

In this study, we use the widely extended Dice Similarity Coefficient (DSC) for the evaluation of the accuracy of non-rigid registration in the task of atlas-based segmentation [48,49]. As a proxy to transformation quality, we measure the invertibility and smoothness of the transformations using different metrics based on the Jacobian determinant of the transformations (in the following, we use the word Jacobian to refer to its determinant). Namely, we use the Jacobian extrema (min and max), the number of negative Jacobians, and the standard deviation of the logarithm of the positive Jacobians (SDlogJ). The Jacobian extrema allow measuring the greatest changes in volume, whether there are foldings in the transformations, and how aggressive they are. The number of negative Jacobians allows measuring whether there is a general tendency to fold, or foldings occur in a few isolated examples. The SDlogJ allows measuring the uniformity of the amount of deformation. In our evaluation, we depart from just showing results of DSC accuracy, or recommending the methods yielding the best DSC metrics. Instead, we analyze the compromise between accuracy and smoothness depending on the values of the regularization parameter α defining operator L in Eq. (2) in a similar way as conducted in [39].

In the last decade, we have witnessed a trend where the evaluation of non-rigid registration is performed exclusively in terms of the DSC accuracy. Some methods have become popular due to their high DSC accuracies, obtained at the expense of reducing smoothness or giving up invertibility. These accuracies are considered the only criterion to prevail over the state of the art. It has been shown that properties such as smoothness, invertibility, or statistics enabling are obtained at the expense of reducing the DSC accuracy. Therefore, it is usual that methods with these desirable properties are reported to be of inferior performance, and the unfair use of DSC accuracy as the only criterion to establish superior performance is not discussed in the evaluations presented in the literature. In [34] we tried to break this inercy proposing the combination of segmentation overlap metrics with different metrics reflecting the smoothness and invertibility of the transformations such as the Jacobian extrema and the number of negative Jacobians. Our proposal justifies the selection of the evaluation metrics used in this work.

4.5. Evaluation results

Table 1 shows the mean and standard deviation of the DSC values after registration and the measurements obtained from the Jacobians. In addition, Fig. 1 shows, in the shape of box and whisker plots, the statistical distribution of the DSC values after averaging across the 32 and 35 segmented structures for NIREP and OASIS, respectively.

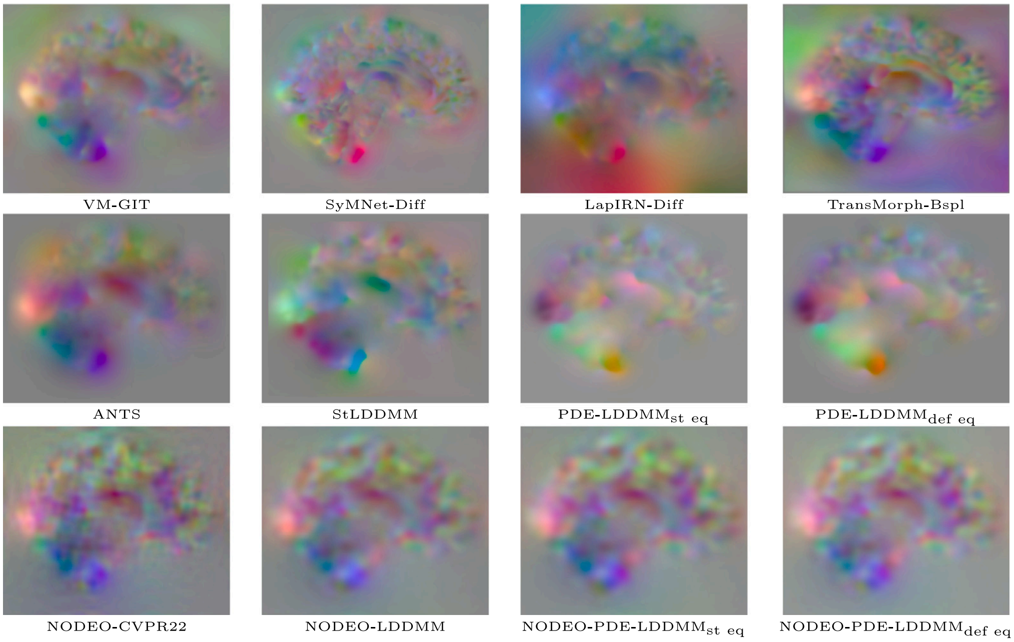
VM-GIT SyMNet-Diff LapIRN-Diff TransMorph-Bspl
ANTS StLDDMM PDE-LDDMM$_{\mathrm{st\ eq}}$ PDE-LDDMM$_{\mathrm{def\ eq}}$
NODEO-CVPR22 NODEO-LDDMM NODEO-PDE-LDDMM$_{\mathrm{st\ eq}}$ NODEO-PDE-LDDMM$_{\mathrm{def\ eq}}$

Fig. 5. NIREP. Sagittal view of the displacement fields in a representative experiment. The RGB color map proposed in VoxelMorph paper is used for the color representation of the vector fields (see Fig. 2). NODEO-LDDMM methods are shown with $\alpha = 0.0005$.

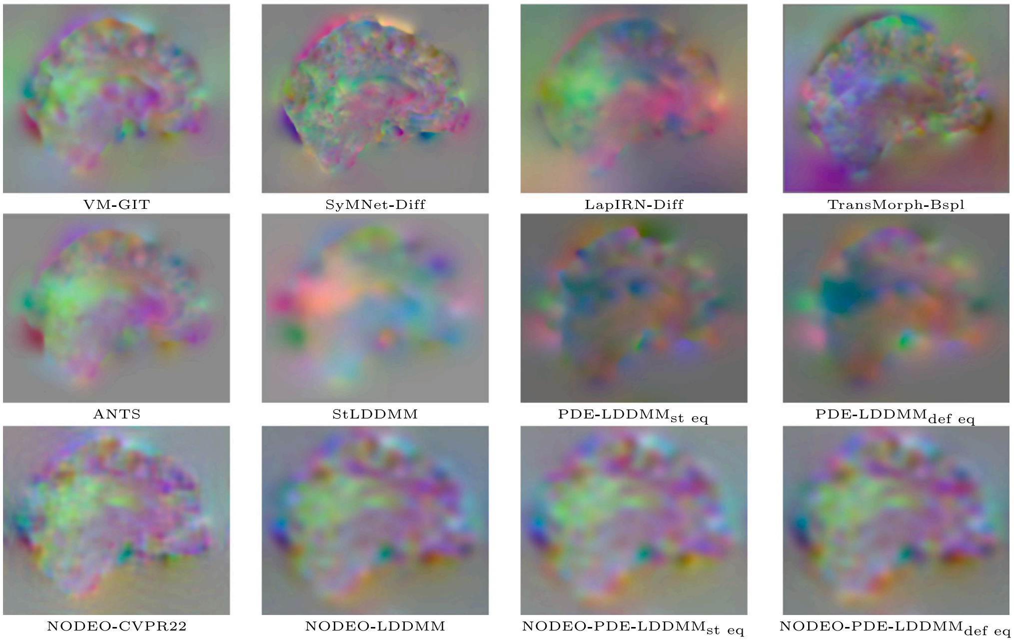
VM-GIT SyMNet-Diff LapIRN-Diff TransMorph-Bspl
ANTS StLDDMM PDE-LDDMM$_{\mathrm{st\ eq}}$ PDE-LDDMM$_{\mathrm{def\ eq}}$
NODEO-CVPR22 NODEO-LDDMM NODEO-PDE-LDDMM$_{\mathrm{st\ eq}}$ NODEO-PDE-LDDMM$_{\mathrm{def\ eq}}$

Fig. 6. OASIS-L2R22. Sagittal view of the displacement fields in a representative experiment. The RGB color map proposed in VoxelMorph paper is used for the color representation of the vector fields (see Fig. 2). NODEO-LDDMM methods with are shown with $\alpha = 0.0010$.

In NIREP database, all NODEO methods with $\alpha \leq 0.0005$ reached or overpassed the baseline established by the best-performing deep-learning and traditional benchmarks in terms of the DSC. The min(J)-max(J) range and the number of negative Jacobians were related to the amount of regularization established with parameter α. The methods with $\alpha = 0.0005$ may yield a good compromise between high DSC and moderate Jacobian values. Although the number of negative Jacobian reaches several hundreds, the minimum Jacobian values indicate that the foldings are not aggressive, leading to nearly diffeomorphic solutions. In this case, our proposed NODEO methods obtain competitive DSC values compared with VoxelMorph and StLDDMM. StLDDMM and NODEO-LDDMM perform similarly, and the two variants of NODEO-PDE-LDDMM overpass PDE-LDDMM variants.

In OASIS database, all NODEO methods with $\alpha \leq 0.0010$ reached or overpassed the baseline of deep-learning and traditional methods in terms of the DSC. In this case, the good compromise between high DSC and moderate Jacobian values is obtained with $\alpha = 0.0010$. The number of negative Jacobians greatly increased with respect to NIREP results. The performance is competitive with the best deep-learning and traditional benchmark methods. Again, the two variants of NODEO-PDE-LDDMM surpassed PDE-LDDMM variants. The differences between OASIS-L2R22 validation and test set in terms of the DSC were similar

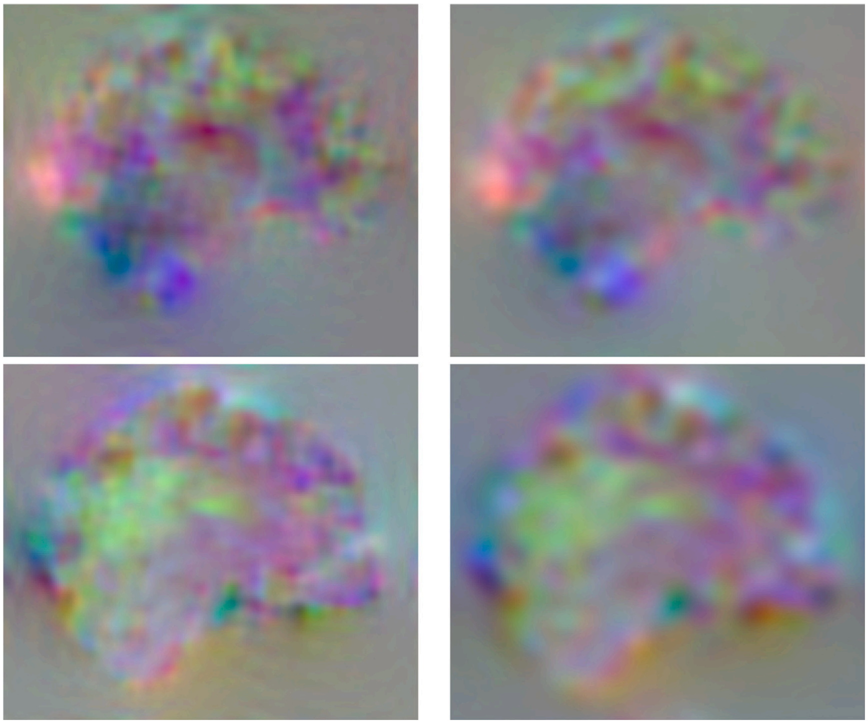

Fig. 7. Zoom of the displacement fields shown in Figs. 5 and 6 for the enhancement of the comparison between NODEO-CVPR22 and NODEO-LDDMM. The artifacts in NODEO-CVPR22 flows are neatly appreciated in the left figures.

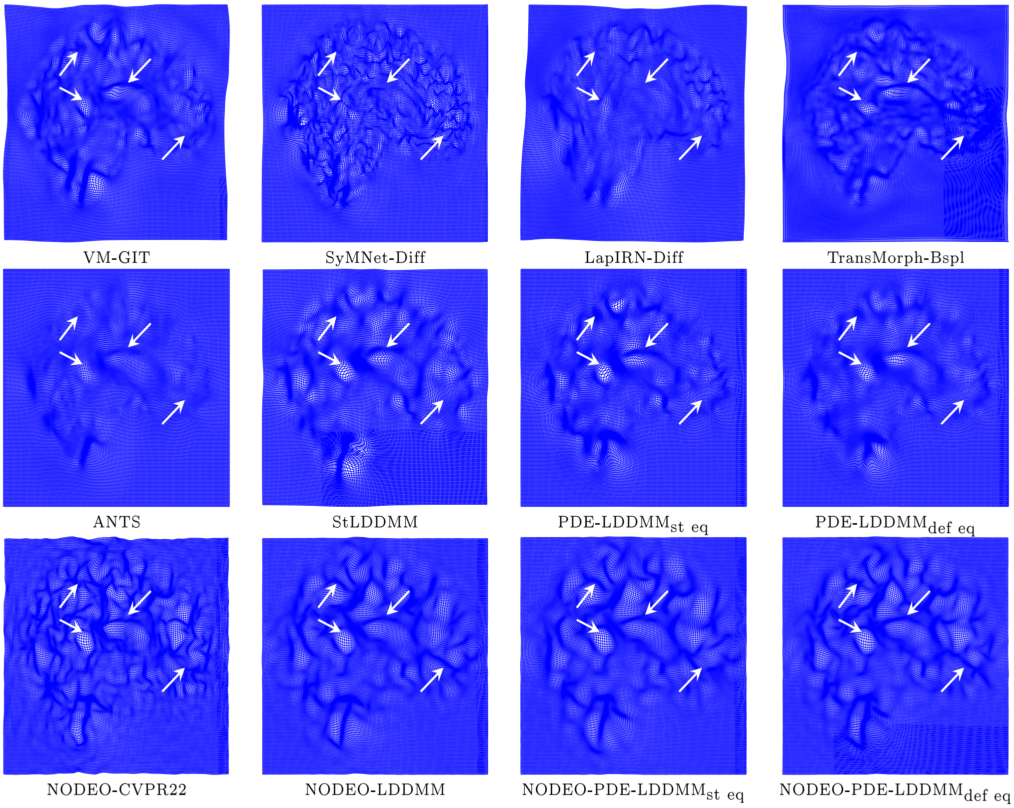

Fig. 8. NIREP. Sagittal view of the transformation grids in a representative experiment. NODEO-LDDMM methods are shown with $\alpha = 0.0005$. The white arrows point out locations where the similarities and differences among the methods can be neatly appreciated.

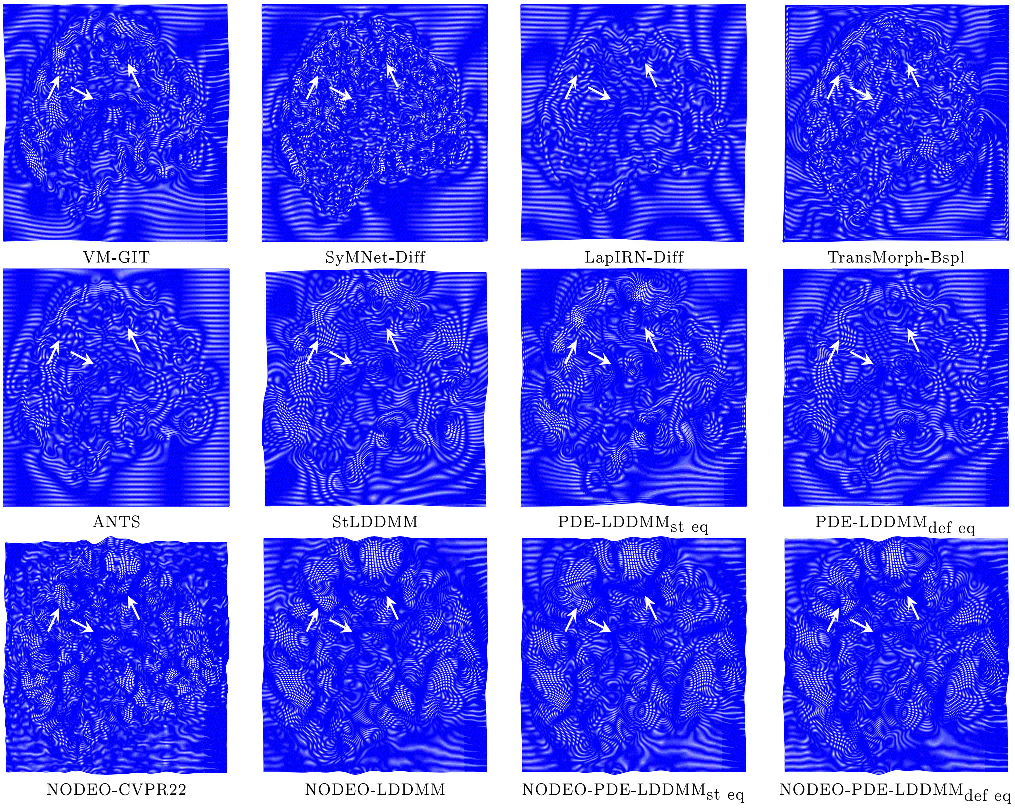

Fig. 9. OASIS-L2R22. Sagittal view of the transformation grids in a representative experiment. NODEO-LDDMM methods are shown with $\alpha = 0.0010$. The white arrows point out locations where the similarities and differences among the methods can be neatly appreciated.

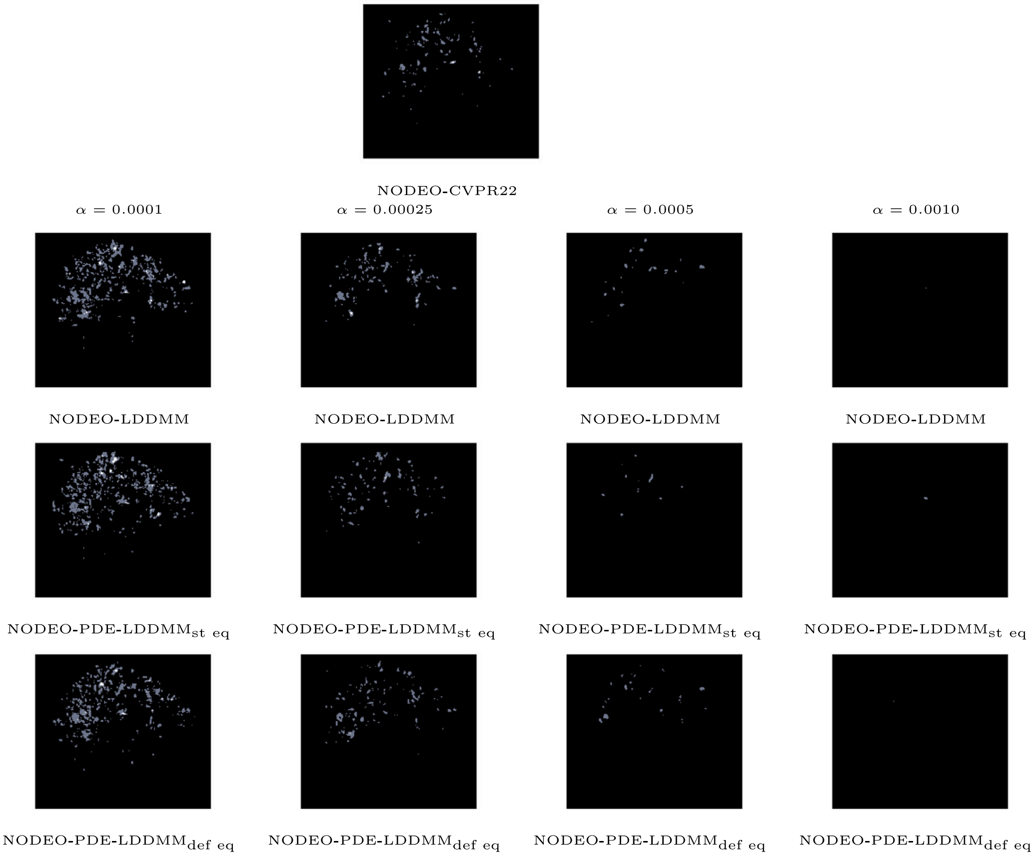

Fig. 10. NIREP. Maximum intensity projection in the sagittal direction of the number of negative Jacobians obtained with NODEO methods through the 15 experiments.

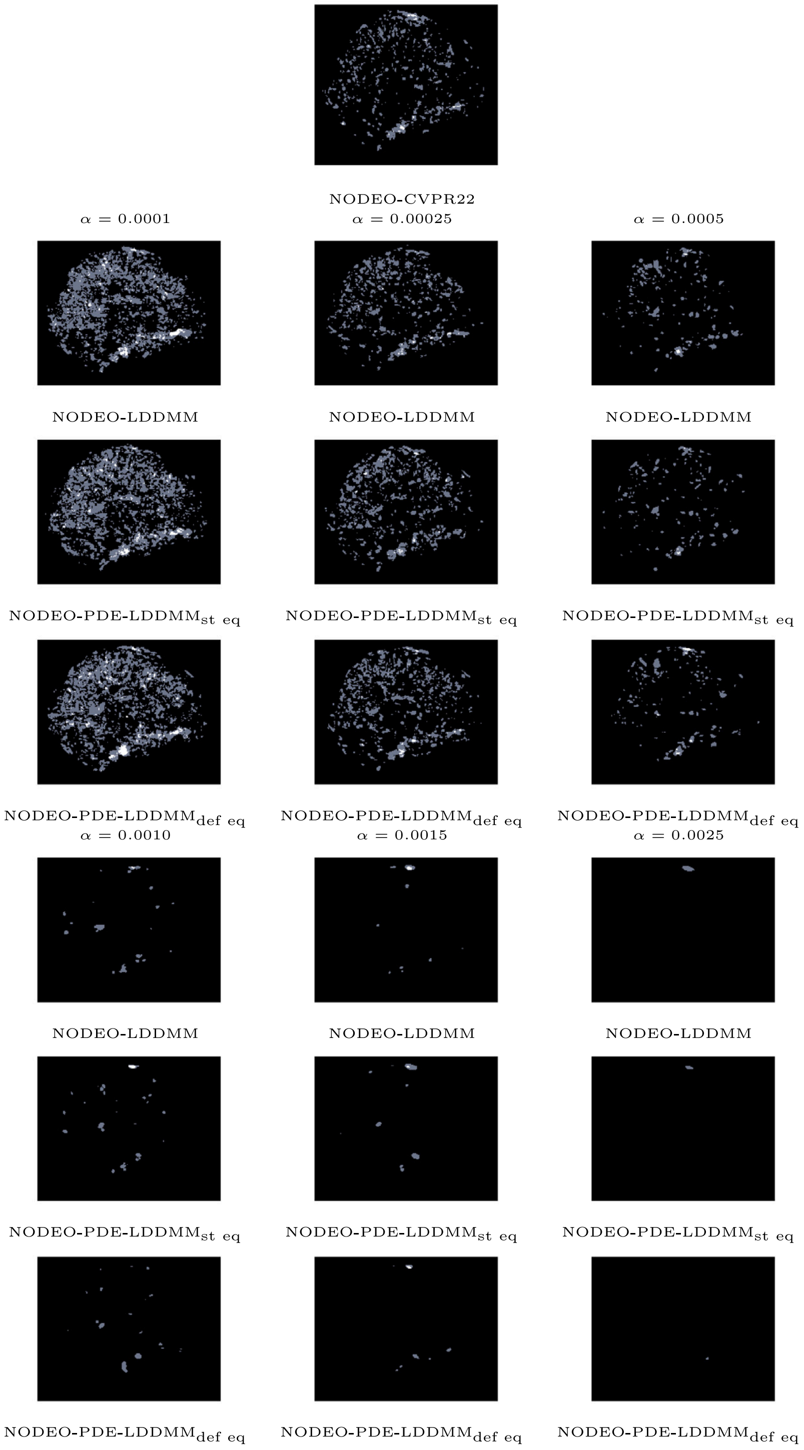

Fig. 11. OASIS-L2R22 validation set. Maximum intensity projection in the sagittal direction of the number of negative Jacobians obtained with NODEO methods through the 19 experiments.

within the methods and consistent across them. The Jacobian extrema remained within a similar min–max range. However, the number of negative Jacobians increased considerably in the test set.

In both NIREP and OASIS, NODEO-CVPR22 outperformed in DSC accuracy our selected configurations. However, this is at the cost of greatly increasing the number of negative Jacobians and the minimum Jacobian values. It is well-known that high regularization constraints reduce the ability of a method from obtaining high DSC values while constraints leading to low regularization facilitate increasing DSC accuracy. The performance of NODEO-CVPR22 in terms of DSC and Jacobians is a consequence of a lower regularization.

4.6. Qualitative results

Apart from the quantitative evaluation, it is important to show some illustrative examples for a qualitative assessment. Figs. 3 and 4 show sagittal views of the differences after registration of the benchmark and our proposed methods for the different α values. The methods

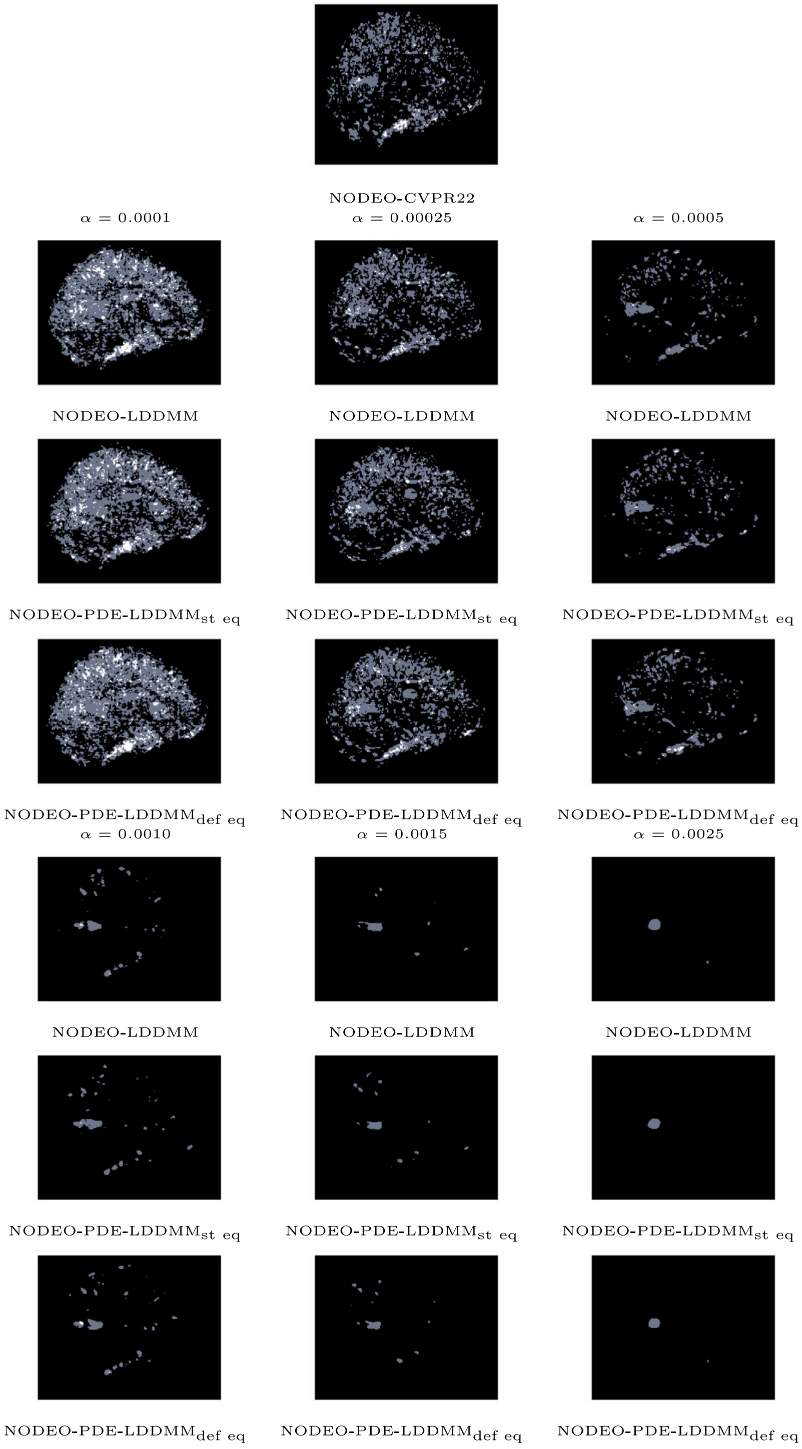

NODEO-CVPR22

$\alpha = 0.0001$ $\alpha = 0.00025$ $\alpha = 0.0005$

NODEO-LDDMM NODEO-LDDMM NODEO-LDDMM

NODEO-PDE-LDDMM$_{\mathrm{st\ eq}}$ NODEO-PDE-LDDMM$_{\mathrm{st\ eq}}$ NODEO-PDE-LDDMM$_{\mathrm{st\ eq}}$

NODEO-PDE-LDDMM$_{\mathrm{def\ eq}}$ NODEO-PDE-LDDMM$_{\mathrm{def\ eq}}$ NODEO-PDE-LDDMM$_{\mathrm{def\ eq}}$

$\alpha = 0.0010$ $\alpha = 0.0015$ $\alpha = 0.0025$

NODEO-LDDMM NODEO-LDDMM NODEO-LDDMM

NODEO-PDE-LDDMM$_{\mathrm{st\ eq}}$ NODEO-PDE-LDDMM$_{\mathrm{st\ eq}}$ NODEO-PDE-LDDMM$_{\mathrm{st\ eq}}$

NODEO-PDE-LDDMM$_{\mathrm{def\ eq}}$ NODEO-PDE-LDDMM$_{\mathrm{def\ eq}}$ NODEO-PDE-LDDMM$_{\mathrm{def\ eq}}$

Fig. 12. OASIS-L2R22 test set. Maximum intensity projection in the sagittal direction of the number of negative Jacobians obtained with NODEO methods through the 39 experiments.

reduce the differences after registration to different extents. Our proposed methods are found within the methods with the smallest visual differences. The intensity differences among the methods can be better appreciated in NIREP database. The deep-learning methods are not able to reduce intensity differences in the parietal lobe. In particular, LapIRN-Diff and TransMorph-Bspl show notable intensity differences all over the cortex, at the parieto-occipital sulcus, and the boundaries of the corpus callosum. Traditional LDDMM methods show intensity differences in a small area close to the central sulcus. The pattern of differences of our proposed methods with $\alpha = 0.0005$ is similar to traditional methods. Differences are mostly located in the parietal lobe and the cortex boundary of the occipital lobe.

Figs. 5 and 6 show sagittal views of the RGB coded maps of the displacement fields of the methods considered in this work. Fig. 2 shows the RGB cube for the interpretation of the colormaps. The visual smoothness of traditional LDDMM methods can be also appreciated in VM-GIT, LapIRN-Diff, and TransMorph-Bspl. While NODEO-CVPR22 flows exhibit artifacts typical of ODE numerical instabilities, our proposed methods do not show such artifacts and the visual smoothness is comparable with their traditional counterparts (see Fig. 7). In OASIS, it drives our attention the boundary artifact shown by the displacement fields of the deep-learning methods in the cortex boundary of the parietal and frontal lobes.

Figs. 8 and 9 show sagittal views of the transformation grids. The visual exploration and zooming of the transformation grids is even more informative than the visualization of the displacement fields. Strong qualitative differences can be neatly appreciated in the figures. White arrows point out some relevant ones. We can appreciate that the deformation of traditional methods are concentrated in the central brain structures, such as the corpus callosum, caudate nucleus, and the ventricles. NODEO-CVPR22, NODEO-LDDMM, and NODEO-PDE-LDDMM specialize in obtaining deformations not only in the central structures but also all over the cortex, a challenging location for non-rigid registration. Their patterns of deformation greatly differ from their corresponding traditional methods. The transformations shown by NODEO-CVPR22 in the corpus callosum region or the frontal region seem much less plausible than the transformations shown by our proposed methods. The patterns of deformation in VM-GIT look much more similar to StLDDMM and PDE-LDDMM than any of the NODEO methods. This ability to capture deformations in the cortex could be one of the reasons for the exceptional DSC accuracy shown in NIREP evaluation.

Last, but not least, Figs. 10, 11, and 12 depict the locations of the negative Jacobians obtained with NODEO methods throughout all the registration experiments represented as maximum intensity projections of an image displaying the count of negative Jacobians in the sagittal direction. For NIREP, the negative Jacobians are primarily situated in the cortex, a challenging region for diffeomorphic registration. Compared with NODEO-CVPR22, the distribution of negative Jacobians for our NODEO methods is reduced for our recommended $\alpha = 0.0005$. For OASIS-L2R22, NODEO-CVPR22 shows negative Jacobians spread across the entire image. For our NODEO methods, the distribution of negative Jacobians is significantly decreased for our recommended $\alpha = 0.0010$.

4.7. Computational complexity

To give closure to our analysis, we show in Table 2 the time and memory requirements of our proposed methods in comparison with the benchmark methods. Regarding the memory requirements, NODEO-CVPR22 and NODEO-LDDMM show similar values. They are of the same order as LapIRN-Diff and PDE-LDDMM. On the contrary, the memory requirements of both variants of NODEO-PDE-LDDMM rise to the order of 10 GBs. Regarding time requirements, NODEO-CVPR22 and NODEO-LDDMM take around one minute, while StLDDMM take around half a minute. The PDE-LDDMM version of NODEO-PDE-LDDMM st eq takes around 68 s less. However, the PDE-LDDMM version of PDE-LDDMM def eq is less efficient with around 71 s more. Thus, our proposed NODEO-LDDMM can be considered a time-efficient method with reasonable memory consumption. From NODEO-PDE-LDDMM, the variant based on the deformation equation outperforms the time efficiency of PDE-LDDMM methods. We will explore in future work the improvement in complexity yielded by the band-limited parametrization.

5. Conclusions

In this paper, we have introduced three different methods at the intersection of LDDMM and PDE-LDDMM families and deep-learning: NODEO-LDDMM, NODEO-PDE-LDDMM$_{\text{st eq}}$, and NODEO-PDE-LDDMM$_{\text{def eq}}$. By blending the well-established mathematical formulation of LDDMM with the adaptability of NODEs to learn the solutions of the ordinary differential equations, our proposed methods have bridged gaps regarding optimization robustness and accuracy from traditional methods, and training complexity and generalization capability from learning.

Our method has been evaluated in NIREP and OASIS-L2R22, two datasets posing complementary challenges to the non-rigid registration problem. NIREP provides manual segmentations while OASIS-L2R22 provides automatically segmented structures. The results of our evaluation reveal that our proposed methods are able to compete with traditional LDDMM and deep-learning-based techniques. Our qualitative assessment has shown the superiority obtained with respect to NODEO-CVPR22. Although our results show a solid proof of the potential of our methods in the problem of non-rigid registration, we believe that regularization could be improved in order to get better control over the number of negative Jacobians without reducing accuracy.

The main difference between NODEO methods and deep-learning methods such as VoxelMorph, SymNet, LapIRN, or TransMorph is that the neural networks in NODEO are specific for the given image pair while deep-learning methods intensively train on a large dataset of image pairs, and the resulting neural networks are intended for computing the solution for every test image pair. In terms of computational efficiency, the inference of deep-learning methods is in the order of seconds while the inference of NODEO methods is in the order of minutes. However, NODEO methods are much easier to train. Monitoring training gives information on the performance of the model for the specific image pair. Indeed, the time complexity for NODEO methods is in the order of minutes while for deep-learning methods it ranges from hours to days. The memory complexity is much lower for NODEO than deep-learning methods (the memory for training a batch size of 1 is close to 24 GBs for VoxelMorph). Indeed, NODEO methods are optimizing the networks specifically for the image pair. Therefore, they have much greater generalization ability than deep-learning methods. Increasing the generalization ability in deep-learning methods goes through either training in a larger database or performing instance optimization [50] and, in both cases, this is at the expense of facing the problems with training complexity.

In future work, we will explore ways to increase the regularization. We will also work on the extension of our methods from the stationary to the non-stationary parametrization. This will involve adding the temporal dimension to the networks and developing time-varying NODEs in our methods. These enhancements will allow our systems to better capture the evolution of the dynamics of the velocity fields over time. We anticipate that the resulting models will offer great flexibility and adaptability in addressing challenging image registration scenarios.

Moreover, we will explore the inclusion of physically meaningful constraints in our NODEO-PDE-LDDMM framework, such as incompressibility [13]. This will require the integration of physical laws (such as conservation of mass) into the loss function, ensuring that the learned dynamics respect the fundamental principles of physics. Techniques like Lagrange multipliers or penalty losses could be used to enforce incompressibility constraints during training. Furthermore, we will investigate how these constraints can be generalized to other physical properties, to make our PDE-LDDMM approach applicable in different contexts. We believe that incorporating these physically informed elements will not only improve the performance of our methods but also increase their robustness, making them applicable to a broad range of clinical problems.

Declaration of competing interest

The authors declare that they have no known competing financial interests or personal relationships that could have appeared to influence the work reported in this paper.

Acknowledgments

The authors sincerely thank the anonymous reviewers for their valuable feedback and suggestions, which have greatly enhanced the quality of this work. We also would like to acknowledge the authors of the deep-learning methods and the owners of NIREP and

Table 3
Scheme with the evolution of our proposed methods from the original NODEO proposal [23].

$$\begin{tikzcd}
 & & \text{NODEO-PDE-LDDMM}_{\text{st eq}} \\
\text{NODEO-CVPR22} \arrow[r, "\mathcal{L}_{\text{lddmm}}=\int_0^1 \|v_t^\theta(\phi_{t,0})\|_V^2\,dt"] & \text{NODEO-LDDMM} \arrow[ru, bend left, "m \text{ and } \lambda"] \arrow[rd, bend right, "\partial_t\phi_{t,0}+D\phi_{t,0}v_t=0"'] & \\
 & & \text{NODEO-PDE-LDDMM}_{\text{def eq}}
\end{tikzcd}$$

OASIS datasets for the publication of the models and data. We thank Ubaldo Ramon-Julvez for valuable advise during the code implementation phase. This work was partially supported by the national research grants PID2019-104358RB-I00 (DL-Ageing project), PID2022-138703OB-I00 (Trust-B-EyE project), RICORS network of inflammatory diseases RD24/0007/0022 form Carlos III Health Institute, Government of Aragon grant PROY_B50_24, and Government of Aragon Group Reference T64_23R (COS2MOS research group). The funders had no role in study design, data collection and analysis, decision to publish, or preparation of the manuscript.

Appendix A. Methodological landscape of our proposed methods

Table 3 shows a diagram of the methodological landscape of our proposed methods illustrating the main differences between NODEO-CVPR22 and NODEO-LDDMM and between NODEO-LDDMM and NODEO-PDE-LDDMM.

Appendix B. Algorithms

Algorithms 1 and 2 gather the steps for a gradient-descent version of LDDMM and NODEO-LDDMM. Both algorithms share common steps such as the computation of $\phi_{t,0}^{n+1}$, $I_0 \circ \phi_{t,0}$, and the energy values. However, in the case of LDDMM the solution of the transport equation is approached using Semi-Lagrangian or Scaling and Squaring solvers [16, 51,52]. In the case of NODEO, the solution is approached using Euler solvers, and the right-hand-side of the equation is computed from the NODE neural representation. The other fundamental difference is in the optimization. In the case of LDDMM, the energy gradient is computed from the expression analytically derived in [5] and used in the update of v_t. In the case of NODEO, the loss gradient is computed using automatic differentiation and used to perform backpropagation and update the neural representation of $-v_t^\theta(\phi_{t,0})$.

Algorithms 3 and 4 gather the steps for both variants of our NODEO-PDE-LDDMM. Using the algorithm of NODEO-LDDMM as a backbone, the algorithms compute the ingredients needed in the computation of v_t and backpropagation leads to the update of the right-hand-side of the ODEs involved in both approaches.

Algorithm 1. LDDMM.

```
Data: $I_0, I_1, v_t^0 \in V, L, K, \sigma, \epsilon$.
Results: $v_t \in V$, arg min of Eq 1.
for $n \leftarrow 0$ to convergence do
  1) Compute $\phi_{t,0}^{n+1}(t)$ from the corresponding transport equation.
  2) Compute $I_0 \circ \phi_{t,0}$ from $I_0$ and $\phi_{t,0}^{n+1}(t)$.
  3) Compute $|D\phi_{t,1}|$.
  4) Compute $\nabla_v E(v)$ from Eq 6.
  5) Compute $v_t^{n+1} = v_t^n - \epsilon \nabla_v E(v_t)$.
  6) Compute the image similarity, the regularization energy, and the global energy and check for algorithm convergence. Apply the selected line-search strategy.
end
```

Algorithm 2. NODEO-LDDMM.

```
Data: $I_0, I_1, (v_t^\theta)^0, L, K, \sigma, n_{its}$.
Results: $-v_t^\theta(\phi_{t,0})$, arg min of Eq 12, $\phi_{t,0}$, solution of Eq 11 through the NODE solver.

Build the NODE network. Initialize randomly $-v_t^\theta(\phi_{t,0})$.
for $n \leftarrow 0$ to $n_{its}$ do
  1) Compute $\phi_{t,0}^{n+1}$ from Eq 11.
  2) Compute $-v_t(\phi_{t,0})$ from $-v_t^\theta(\phi_{t,0})$.
  3) Compute $I_0 \circ \phi_{t,0}$ from $I_0$ and $\phi_{t,0}^{n+1}$ using a spatial transformer.
  4) Compute the image similarity, the regularization losses, and the loss function.
  5) Perform backward propagation on $-v_t^\theta(\phi_{t,0})$.
  6) Update $(-v_t^\theta(\phi_{t,0}))^{n+1}$.
end
Select the best-performing $-v_t^\theta(\phi_{t,0})$ according to the stopping strategy.
```

Algorithm 3. NODEO-PDE-LDDMM$_{\text{st eq}}$.

```
Data: $I_0, I_1, ((D\phi_{t,0} \cdot v_t)^\theta)^0, ((D\phi_{0,t} \cdot v_t)^\theta)^0, L, K, \sigma, n_{its}$.
Results: $v_t$, arg min of Eq 18 with lNCC metric, $\phi_{t,0}$ and $\phi_{0,t}$, solutions of Eq 22 through the NODE solvers.

Build the NODE network. Initialize randomly $(D\phi_{t,0} \cdot v_t)^\theta$ and $(D\phi_{0,t} \cdot v_t)^\theta$.
for $n \leftarrow 0$ to $n_{its}$ do
  1) Compute $\phi_{t,0}^{n+1}$ and $\phi_{0,t}^{n+1}$ through the NODE solvers.
  2) Compute $m(t)$ from Eq 23 using a spatial transformer.
  3) Compute $\lambda(t)$ from Eq 23 using a spatial transformer.
  4) Compute $v(t)$ from Eq 26.
  5) Compute the image similarity, the regularization losses, and the loss function.
  6) Perform backward propagation on $(D\phi_{t,0} \cdot v_t)^\theta$ and $(D\phi_{0,t} \cdot v_t)^\theta$.
  7) Update $((D\phi_{t,0} \cdot v_t)^\theta)^{n+1}$ and $((D\phi_{0,t} \cdot v_t)^\theta)^{n+1}$.
end
Select the best-performing $((D\phi_{t,0} \cdot v_t)^\theta)^{n+1}$ and $((D\phi_{0,t} \cdot v_t)^\theta)^{n+1}$ according to the stopping strategy and provide as solution the associated $v_t$.
```

Algorithm 4. NODEO-PDE-LDDMM$_{\text{def eq}}$.

```
Data: $I_0, I_1, ((D\phi_{t,0} \cdot v_t)^\theta)^0, ((\nabla \cdot (\rho_t \cdot v_t))^\theta)^0, L, K, \sigma, n_{its}$.
Results: $v_t$, arg min of Eq 18 with lNCC metric and $\phi_t$ solution of Eq 22 through the NODE solver.

Build the NODE network. Initialize randomly $(D\phi_{t,0} \cdot v_t)^\theta$ and $(\nabla \cdot (\rho_t \cdot v_t))^\theta$.
for $n \leftarrow 0$ to $n_{its}$ do
  1) Compute $\phi_{t,0}^{n+1}$ through the NODE solver.
  2) Compute $\rho(1)$ from Eq 24 using a spatial transformer for $m(1)$.
  3) Compute $\rho(t)$ through the NODE solver.
  4) Compute $v(t)$ from Eq 27.
  5) Compute the image similarity, the regularization losses, and the loss function.
  6) Perform backward propagation on $(D\phi_{t,0} \cdot v_t)^\theta$ and $(\nabla \cdot (\rho_t \cdot v_t))^\theta$.
  7) Update $((D\phi_{t,0} \cdot v_t)^\theta)^{n+1}$ and $((\nabla \cdot (\rho_t \cdot v_t))^\theta)^{n+1}$.
end
Select the best-performing $((D\phi_{t,0} \cdot v_t)^\theta)^{n+1}$ and $((\nabla \cdot (\rho_t \cdot v_t))^\theta)^{n+1}$ according to the stopping strategy and provide as solution the associated $v_t$.
```

Appendix C. Regularization in LDDMM and NODEO-LDDMM

In our study, regularization parameters were selected from a search of the optimal parameter α in NIREP and OASIS-L2R22 datasets. In this appendix, we present the details of the study conducted for such selection. Table 4 shows the quantitative results in LDDMM and PDE-LDDMM for the different values of the regularization parameter α.

In NIREP, the highest DSC values are obtained with $\alpha = 0.0005$ or $\alpha = 0.0010$. However, looking at the Jacobian metrics we appreciate that the regularization is too weak and some variants of the methods

Table 4
LDDMM and PDE-LDDMM. Quantitative results on NIREP and OASIS-L2R22 for the selection of the regularization parameter α. Mean and standard deviation of the Dice Similarity Coefficient (DSC), maximum and minimum of the Jacobian determinant, number of negative Jacobian determinants, and standard deviation of the logarithm of the Jacobian determinant for those points with positive values. The abbreviation st eq is used for the PDE-LDDMM method based on the state equation. The abbreviation def eq is used for the PDE-LDDMM method based on the deformation equation. The arrows indicate that high DSC values while not extreme Jacobian determinant values are preferable. In the column failed J we indicate the number of experiments with failed Jacobian computation (extremely large $max(J)$ values, > 1000, or nan) due to numerical issues with low regularization. These values were removed from the computation of the corresponding Jacobian-based quantitative results.

NIREP								
Method	Metric	α	DSC (%) ↑	max (J) ↓	min (J) ↑	# of $\lvert J_\phi \rvert \le 0$ ↓	SDlogJ ↓	failed J
Stationary LDDMM	lNCC	0.0005	63.39 ± 1.62	–	–	–	–	15
Stationary LDDMM	lNCC	0.0010	62.10 ± 1.54	15.09 ± 4.46	0.02 ± 0.22	39	0.27 ± 0.01	–
Stationary LDDMM	lNCC	0.0015	60.85 ± 1.47	15.09 ± 4.46	0.02 ± 0.22	0	0.27 ± 0.01	–
Stationary LDDMM	lNCC	0.0025	58.98 ± 1.30	8.03 ± 1.94	0.19 ± 0.08	0	0.21 ± 0.01	–
PDE-LDDMM st eq	lNCC	0.0005	60.39 ± 2.46	11.78 ± 8.41	0.00 ± 0.01	0	0.24 ± 0.02	–
PDE-LDDMM st eq	lNCC	0.0010	60.11 ± 2.81	7.41 ± 3.56	0.01 ± 0.01	0	0.23 ± 0.02	–
PDE-LDDMM st eq	lNCC	0.0015	60.19 ± 2.64	6.37 ± 2.43	0.02 ± 0.02	0	0.22 ± 0.02	–
PDE-LDDMM st eq	lNCC	0.0025	59.84 ± 2.53	5.17 ± 1.64	0.02 ± 0.02	0	0.21 ± 0.02	–
PDE-LDDMM def eq	NCC	0.0005	59.41 ± 4.47	9.56 ± 3.47	0.06 ± 0.03	0	0.23 ± 0.03	1
PDE-LDDMM def eq	NCC	0.0010	60.92 ± 1.88	15.59 ± 5.89	0.05 ± 0.03	0	0.24 ± 0.03	–
PDE-LDDMM def eq	NCC	0.0015	60.67 ± 2.38	29.95 ± 33.66	0.05 ± 0.03	0	0.24 ± 0.01	–
PDE-LDDMM def eq	NCC	0.0025	60.10 ± 1.45	13.19 ± 10.59	0.09 ± 0.03	0	0.21 ± 0.01	–
OASIS-L2R22								
Method	Metric	α	DSC (%) ↑	max (J) ↓	min (J) ↑	# of $\lvert J_\phi \rvert \le 0$ ↓	SDlogJ ↓	failed J
Stationary LDDMM	lNCC	0.0005	78.55 ± 3.20	1062.09 ± 1065.20	-217.73 ± 287.48	39 300	0.63 ± 0.12	–
Stationary LDDMM	lNCC	0.0010	78.35 ± 3.20	227.49 ± 235.54	-14.89 ± 41.82	6578	0.41 ± 0.06	–
Stationary LDDMM	lNCC	0.0015	78.15 ± 2.87	75.27 ± 132.66	-1.11 ± 1.42	2729	0.34 ± 0.04	–
Stationary LDDMM	lNCC	0.0025	77.47 ± 2.81	32.16 ± 70.55	-0.52 ± 1.05	2976	0.30 ± 0.05	–
PDE-LDDMM st eq	lNCC	0.0005	73.64 ± 2.99	33.00 ± 45.70	0.00 ± 0.00	76	0.27 ± 0.04	3
PDE-LDDMM st eq	lNCC	0.0010	71.19 ± 10.73	16.85 ± 12.67	0.00 ± 0.00	0	0.26 ± 0.04	3
PDE-LDDMM st eq	lNCC	0.0015	72.35 ± 7.13	11.63 ± 7.13	0.00 ± 0.01	0	0.26 ± 0.03	1
PDE-LDDMM st eq	lNCC	0.0025	73.30 ± 5.32	11.51 ± 6.83	0.00 ± 0.01	0	0.26 ± 0.04	1
PDE-LDDMM def eq	NCC	0.0005	74.33 ± 6.19	533.71 ± 267.12	0.02 ± 0.01	0	0.32 ± 0.03	9
PDE-LDDMM def eq	NCC	0.0010	77.07 ± 2.72	116.90 ± 71.31	0.02 ± 0.02	0	0.30 ± 0.02	8
PDE-LDDMM def eq	NCC	0.0015	77.14 ± 2.64	147.54 ± 159.86	0.04 ± 0.02	0	0.27 ± 0.02	4
PDE-LDDMM def eq	NCC	0.0025	76.12 ± 2.61	47.39 ± 80.02	0.08 ± 0.03	0	0.22 ± 0.02	–

show failed Jacobian computations, which is not desirable. From this analysis, we selected $\alpha = 0.0010$.

In OASIS-L2R22, PDE-LDDMM methods obtain the highest DSC values with $\alpha = 0.0005$ or $\alpha = 0.0015$, while StLDDMM obtains the highest DSC values with $\alpha = 0.0005$. PDE-LDDMM is a fragile method where the numerics for the computation of the Jacobian may explode when using weak regularization parameters. Since the obtained DSC values are still competitive with the best-performing regularizations, we selected $\alpha = 0.0025$ as an optimal regularization parameter.

In the case of NODEO based methods, we did not experience failed Jacobian computations in any of the methods, even for $\alpha = 0.0001$, which provided the weakest regularization. Therefore, the use of NODEs in PDE-LDDMM yields a more robust optimization.

In addition, it drives our attention that the range for α selection in NIREP should be between 0.0025 and 0.0005 for LDDMM, between 0.0010 and 0.0001 for NODEO-LDDMM and NODEO-PDE-LDDMM. In OASIS-L2R22, the range changes between 0.0025 and 0.00025. Therefore, the estimations of acceptable regularization ranges in LDDMM cannot be extended to NODEO and viceversa.

Data availability

Data will be made available on request.

References

[1] M.I. Miller, Computational anatomy: shape, growth, and atrophy comparison via diffeomorphisms, Neuroimage 23 (2004) 19–33, http://dx.doi.org/10.1016/j.neuroimage.2004.07.021.

[2] M.I. Miller, A. Qiu, The emerging discipline of computational functional anatomy, Neuroimage 45 (1) (2009) 16–39, http://dx.doi.org/10.1016/j.neuroimage.2008.10.044.

[3] A. Sotiras, C. Davatzikos, N. Paragios, Deformable medical image registration: A survey, IEEE Trans. Med. Imaging 32 (7) (2013) 1153–1190, http://dx.doi.org/10.1109/TMI.2013.2265603.

[4] B.K. Horn, B.G. Schunck, Determining optical flow, Artificial Intelligence 17 (1981) 185–203, http://dx.doi.org/10.1016/0004-3702(81)90024-2.

[5] M.F. Beg, M.I. Miller, A. Trouve, L. Younes, Computing large deformation metric mappings via geodesic flows of diffeomorphisms, Int. J. Comput. Vis. 61 (2) (2005) 139–157, http://dx.doi.org/10.1023/B:VISI.0000043755.93987.aa.

[6] M.I. Miller, S. Arguillere, D.J. Tward, L. Younes, Computational anatomy and diffeomorphometry: A dynamical systems model of neuroanatomy in the soft condensed matter continuum, WIREs Syst. Biol. Med. 10 (6) (2018) http://dx.doi.org/10.1002/wsbm.1425.

[7] X. Pennec, S. Sommer, P.T. Fletcher, Riemannian Geometric Statistics in Medical Image Analysis, Academic Press, 2018, http://dx.doi.org/10.1016/C2017-0-01561-6.

[8] B.B. Avants, N.J. Tustison, G. Song, P.A. Cook, A. Klein, J.C. Gee, A reproducible evaluation of ANTs similarity metric performance in brain image registration, Neuroimage 54 (3) (2011) 2033–2044, http://dx.doi.org/10.1016/j.neuroimage.2010.09.025.

[9] T. Vercauteren, X. Pennec, A. Perchant, N. Ayache, Diffeomorphic demons: Efficient non-parametric image registration, Neuroimage 45 (1) (2009) S61–S72, http://dx.doi.org/10.1016/j.neuroimage.2008.10.040.

[10] X. Pennec, P. Cachier, N. Ayache, Understanding the Demon's algorithm: 3D non-rigid registration by gradient descent, in: Proc. of the 2nd International Conference on Medical Image Computing and Computer Assisted Intervention, MICCAI'99, in: Lecture Notes in Computer Science (LNCS), vol. 1679, Springer- Verlag, Berlin, Germany, 1999, pp. 597–605, http://dx.doi.org/10.1007/10704282_64.

[11] G.L. Hart, C. Zach, M. Niethammer, An optimal control approach for deformable registration, in: Proc. of the IEEE Computer Society Conference on Computer Vision and Pattern Recognition, CVPR'09, 2009, http://dx.doi.org/10.1109/CVPRW.2009.5204344.

[12] A. Mang, G. Biros, An inexact Newton-Krylov algorithm for constrained diffeomorphic image registration, SIAM J. Imaging Sci. 8 (2) (2015) 1030–1069, http://dx.doi.org/10.1137/140984002.

[13] A. Mang, G. Biros, Constrained H1 regularization schemes for diffeomorphic image registration, SIAM J. Imaging Sci. 9 (3) (2016) 1154–1194, http://dx.doi.org/10.1137/15M1010919.

[14] P. Ruhnau, C. Schnorr, Optical Stokes flow estimation: an imaging-based control approach, Exp. Fluids 42 (2007) 61–78, http://dx.doi.org/10.1007/s00348-006-0220-z.

[15] A. Mang, L. Ruthotto, A Lagrangian Gauss Newton Krylov solver for mass- and intensity-preserving diffeomorphic image registration, SIAM J. Sci. Comput. 39 (5) (2017) B860 – B885, http://dx.doi.org/10.1137/17M1114132.

[16] M. Hernandez, Gauss-Newton inspired preconditioned optimization in large deformation diffeomorphic metric mapping, Phys. Med. Biol. 59 (20) (2014) 6085–6115, http://dx.doi.org/10.1088/0031-9155/59/20/6085.

[17] M. Zhang, T. Fletcher, Fast diffeomorphic image registration via Fourier-approximated Lie algebras, Int. J. Comput. Vis. (2018) http://dx.doi.org/10.1007/s11263-018-1099-x.

[18] A. Dosovitskiy, et al., FlowNet: Learning optical flow with convolutional networks, in: Proc. of the 14th IEEE International Conference on Computer Vision, ICCV'15, 2015, http://dx.doi.org/10.1109/ICCV.2015.316.

[19] M.-M. Rohe, M. Datar, T. Heimann, M. Sermesant, X. Pennec, SVF-Net: Learning deformable image registration using shape matching, in: Proc. of the 20th International Conference on Medical Image Computing and Computer Assisted Intervention, MICCAI'17, in: Lecture Notes in Computer Science (LNCS), Springer-Verlag, Berlin, Germany, 2017, pp. 266–274, http://dx.doi.org/10.1007/978-3-319-66182-7_31.

[20] X. Yang, R. Kwitt, M. Styner, M. Niethammer, Quicksilver: Fast predictive image registration - a deep learning approach, Neuroimage 158 (2017) 378–396, http://dx.doi.org/10.1016/j.neuroimage.2017.07.008.

[21] G. Balakrishnan, A. Zhao, M. Sabuncu, A. Dalca, J. Guttag, An unsupervised learning model for deformable medical image registration, in: Proc. of the IEEE Computer Society Conference on Computer Vision and Pattern Recognition, CVPR'18, 2018, pp. 9252–9260, http://dx.doi.org/10.1109/CVPR.2018.00964.

[22] G. Balakrishnan, A. Zhao, M. Sabuncu, J. Guttag, A. Dalca, VoxelMorph: A learning framework for deformable medical image registration, IEEE Trans. Med. Imaging 38 (8) (2019) 1788–1800, http://dx.doi.org/10.1109/TMI.2019.2897538.

[23] Y. Wu, T.Z. Jiahao, J. Wang, P.A. Yushkevich, M.A. Hsieh, J.C. Gee, NODEO: A neural ordinary differential equation based optimization framework for deformable image registration, in: Proc. of the IEEE Computer Society Conference on Computer Vision and Pattern Recognition, CVPR'22, 2022, pp. 20804–20813, http://dx.doi.org/10.1109/CVPR52688.2022.02014.

[24] R.T.Q. Chen, Y. Rubanova, J. Bettencourt, D.K. Duvenaud, Neural ordinary differential equations, in: Proc. of Conference on Neural Information Processing Systems, NEURIPS'18, Vol. 31, 2018, http://dx.doi.org/10.48550/arXiv.1806.07366.

[25] S.A. Faroughi, N.M. Pawar, C. Fernandes, M. Raissi, S. Das, N.K. Kalantari, S. Kourosh-Mahjour, Physics-guided, physics-informed, and physics-encoded neural networks and operators in scientific computing: Fluid and solid mechanics, ASME J. Comput. Inf. Sci. Eng. 24 (4) (2024) 040802, http://dx.doi.org/10.1115/1.4064449.

[26] M. Hernandez, A comparative study of different variants of Newton-Krylov PDE-constrained Stokes-LDDMM parameterized in the space of band-limited vector fields, SIAM J. Imaging Sci. 12 (2) (2019) http://dx.doi.org/10.1137/18M119531.

[27] J. Modersitzki, FAIR: Flexible Algorithms for Image Registration, SIAM, 2009.

[28] T. Polzin, M. Niethammer, M.P. Heinrich, H. Handels, J. Modersitzki, Memory efficient LDDMM for lung CT, in: Proc. of the 19th International Conference on Medical Image Computing and Computer Assisted Intervention, MICCAI'18, in: Lecture Notes in Computer Science (LNCS), Springer- Verlag, Berlin, Germany, 2014, pp. 28–36, http://dx.doi.org/10.1007/978-3-319-46726-9_4.

[29] M. Hernandez, U. Ramon-Julvez, D.S. Tome, Partial differential equation-constrained diffeomorphic registration from sum of squared differences to normalized cross-correlation, normalized gradient fields, and mutual information: A unifying framework, Sensors 22 (2022) 3735, http://dx.doi.org/10.3390/s22103735.

[30] T. Mok, A.C. Chung, Fast symmetric diffeomorphic image registration with convolutional neural networks, in: Proc. of the IEEE Computer Society Conference on Computer Vision and Pattern Recognition, CVPR'20, 2020, pp. 4644–4653, http://dx.doi.org/10.1109/CVPR42600.2020.00470.

[31] T. Mok, A. Chung, Large deformation diffeomorphic image registration with Laplacian pyramid networks, in: Proc. of the 23rd International Conference on Medical Image Computing and Computer Assisted Intervention, MICCAI'20, in: Lecture Notes in Computer Science (LNCS), Springer- Verlag, Berlin, Germany, 2020, http://dx.doi.org/10.1007/978-3-030-59716-0_21.

[32] J. Chen, E.C. Frey, Y. He, W.P. Segars, Y. Li, Y. Du, TransMorph: Transformer for unsupervised medical image registration, Med. Image Anal. 82 (2022) 102615, http://dx.doi.org/10.1016/j.media.2022.102615.

[33] K. He, X. Zhang, S. Ren, J. Sun, Deep residual learning for image recognition, in: Proc. of the IEEE Computer Society Conference on Computer Vision and Pattern Recognition, CVPR'16, 2016, pp. 770–778, http://dx.doi.org/10.1109/CVPR.2016.90.

[34] M. Hernandez, U. Ramon-Julvez, Insights into traditional large deformation diffeomorphic metric mapping and unsupervised deep-learning for diffeomorphic registration and their evaluation, Comput. Biol. Med. 178 (2024) 108761, http://dx.doi.org/10.1016/j.compbiomed.2024.108761.

[35] M. Hoffmann, B. Billot, D. Greve, J. Iglesias, B. Fischl, A. Dalca, SynthMorph: learning contrast-invariant registration without acquired images, IEEE Trans. Med. Imaging 41(3) (2021) 543–558, http://dx.doi.org/10.1109/TMI.2021.3116879.

[36] A. Dosovitskiy, L. Beyer, A. Kolesnikov, D. Weissenborn, X. Zhai, T. Unterthiner, M. Dehghani, M. Minderer, G. Heigold, S. Gelly, J. Uszkoreit, N. Houlsby, An image is worth 16x16 words: Transformers for image recognition at scale, in: Proc. of the International Conference on Learning Representations, ICLR'21, 2021.

[37] J.M. Wolterink, J.C. Zwienenberg, C. Brune, Implicit neural representations for deformable image registration, in: 5th International Conference on Medical Imaging with Deep Learning, MIDL, Vol. 172, 2022, pp. 1349–1359.

[38] K. Han, et al., Diffeomorphic image registration with neural velocity field, in: 2023 IEEE/CVF Winter Conference on Applications of Computer Vision (WACV), Waikoloa, HI, USA, 2023, pp. 1869–1879, http://dx.doi.org/10.1109/WACV56688.2023.00191.

[39] M. Byra, C. Poon, M. Rachmadi, M. Schlachter, H. Skibbe, Exploring the performance of implicit neural representations for brain image registration, Sci. Rep. 13 (2023) 17334, http://dx.doi.org/10.1038/s41598-023-44517-5.

[40] M. Hernandez, Efficient momentum conservation constrained PDE-LDDMM with Gauss–Newton–Krylov optimization, semi-Lagrangian Runge–Kutta solvers, and the band-limited parameterization, J. Comput. Sci. 55 (2021) 101470, http://dx.doi.org/10.1016/j.jocs.2021.101470.

[41] M. Hernandez, Combining the band-limited parameterization and semi-Lagrangian Runge–Kutta integration for efficient PDE-constrained LDDMM, J. Math. Imaging Vision 63 (3) (2021) 555–579, http://dx.doi.org/10.1007/s10851-021-01016-4.

[42] F.X. Vialard, L. Risser, D. Rueckert, C.J. Cotter, Diffeomorphic 3D image registration via geodesic shooting using an efficient adjoint calculation, Int. J. Comput. Vis. 97 (2) (2011) 229–241, http://dx.doi.org/10.1007/s11263-011-0481-8.

[43] G.E. Christensen, X. Geng, J.G. Kuhl, J. Bruss, T.J. Grabowski, I.A. Pirwani, M.W. Vannier, J.S. Allen, H. Damasio, Introduction to the non-rigid image registration evaluation project (NIREP), in: Proc. of 3rd International Workshop on Biomedical Image Registration, WBIR'06, Vol. 4057, 2006, pp. 128–135, http://dx.doi.org/10.1007/11784012_16.

[44] M. Hernandez, Band-limited Stokes large deformation diffeomorphic metric mapping, IEEE J. Biomed. Health Inform. 23 (1) (2019) 362–373, http://dx.doi.org/10.1109/JBHI.2018.2815346.

[45] A. Hering, et al., Learn2Reg: Comprehensive multi-task medical image registration challenge, dataset and evaluation in the era of deep learning, IEEE Trans. Med. Imaging 42 (3) (2023) 697–712, http://dx.doi.org/10.1109/TMI.2022.3213983.

[46] A. Hoopes, M. Hoffmann, B. Fischl, J. Guttag, A. Dalca, Hypermorph: Amortized hyperparameter learning for image registration, in: Proc. of International Conference on Information Processing and Medical Imaging, IPMI'21, in: Lecture Notes in Computer Science (LNCS), vol. 12729, Springer-Verlag, Berlin, Germany, 2021, pp. 3–17, http://dx.doi.org/10.1007/978-3-030-78191-0.

[47] B.B. Avants, C.L. Epstein, M. Grossman, J.C. Gee, Symmetric diffeomorphic image registration with cross-correlation: Evaluating automated labeling of elderly and neurodegenerative brain, Med. Image Anal. 12 (2008) 26–41, http://dx.doi.org/10.1016/j.media.2007.06.004.

[48] A. Klein, et al., Evaluation of 14 nonlinear deformation algorithms applied to human brain MRI registration, Neuroimage 46 (3) (2009) 786–802, http://dx.doi.org/10.1016/j.neuroimage.2008.12.037.

[49] T. Rohlfing, Image similarity and tissue overlaps as surrogates for image registration accuracy: widely used but unreliable, IEEE Trans. Med. Imaging 31 (2) (2012) 153–163, http://dx.doi.org/10.1109/TMI.2011.2163944.

[50] L. Tian, et al., GradICON: Approximate diffeomorphisms via gradient inverse consistency, in: Proc. of the IEEE Computer Society Conference on Computer Vision and Pattern Recognition, CVPR'23, 2023, pp. 18084–18094, http://dx.doi.org/10.1109/CVPR52729.2023.01734.

[51] M.F. Beg, P.A. Helm, E. McVeigh, M.I. Miller, R.L. Winslow, Computational cardiac anatomy using MRI, Magn. Reson. Med. 52 (5) (2004) 1167–1174, http://dx.doi.org/10.1002/mrm.20255.

[52] V. Arsigny, O. Commonwick, X. Pennec, N. Ayache, A log-Euclidean framework for statistics on diffeomorphisms, in: Proc. of the 9th International Conference on Medical Image Computing and Computer Assisted Intervention, MICCAI'06, in: Lecture Notes in Computer Science (LNCS), vol. 4190, Springer- Verlag, Berlin, Germany, 2006, pp. 924–931, http://dx.doi.org/10.1007/11866565_113.

Monica Hernandez obtained her M.Sc. degree in Mathematics from the University of Zaragoza in 2000, followed by a Ph.D. in Computer Science from the same institution in 2008. Since 2011, she has served as an Associate Professor in the Department of Informatics and Systems Engineering. Her research focuses on diffeomorphic registration with traditional and deep-learning methods, Computational Anatomy applications, and interpretable machine learning methods for the early diagnosis of neurodegenerative diseases.